Programmable Self-assembly For Microsystem Integration

Ji Hao Hoo

A dissertation
submitted in partial fulfillment of the
requirements for the degree of

Doctor of Philosophy

University of Washington

2014

Reading Committee:
Karl F. Böhringer, Chair

Rajashree Baskaran

Lih-Yuan Lin

Program Authorized to Offer Degree:
Electrical Engineering

University of Washington

Abstract

Programmable Self-assembly For Microsystem Integration

Ji Hao Hoo

Chair of the Supervisory Committee:
Professor Karl F. Böhringer
Department of Electrical Engineering, Department of Bioengineering

This dissertation studies and improves upon template-based self-assembly processes as a suite of techniques for microsystem integration.

We first provide an updated definition for microscale self-assembly, and provide a framework that separates all self-assembly processes into three distinct phases which can be independently analyzed.

A catalyst-enhanced self-assembly process is then presented, wherein non-participating 'catalyst' components are introduced to a dry-environment batch-assembly process, demonstrating 25 - 50% reduction in acceleration needed to trigger part motion and up to four times increase in concentration of parts in motion due to addition of catalysts. The presence of catalytic parts allows stochastic part-to-trap assemblies to be performed at lower accelerations than without, and thus allow said assemblies to be performed further from the acceleration-levels required to free trapped parts; this reduces the probability of part-disassembly, thus improving assembly yield. A model from chemical kinetics theory is adapted for the analysis of this catalyst-enhanced self-assembly process.

A variation on the prevalent methodology of driving a stochastic assembly process, using vibrations perpendicular to the assembly surface, is then presented. Using a modified actuator that introduces agitations that are in the plane of the assembly surface, unprecedented control of micropart-motion has been achieved; of note, components can be reliability induced into a "walking mode", where components are moved across surfaces in predetermined directions with a surface-hugging motion. Walking modes enables parts to be moved across surfaces and into binding sites, but do not cause trapped components to disassemble due to the suppression of out-of-plane agitation. Repeatable and programmable complete delivery of components into arrays of traps is achieved in open loop and feedback-enhanced configurations. The theoretical study of this template-based assembly method is performed with (370 × 370 × 150 μm^3) test components, and walking modes are statistically characterized and a chemical kinetics inspired model is developed.

Said self-assembly process is then applied on the assembly of 01005 (0.016” × 0.008”, 0.4 mm × 0.2 mm) surface mount technology resistors and capacitors, demonstrating the transportation, self-alignment, and adherence phases of our template-based assembly process.

Finally, the magnetically aided assembly of 01005 surface mount components in a vertical pose is studied by adapting the visual-feedback systems used throughout the thesis work. Electrical performance has been verified, and our process is demonstrated to be competitive against integrated passive elements in terms of area-footprint and capacitive and resistive property-tolerances.

TABLE OF CONTENTS

Page

LIST OF FIGURES

LIST OF TABLES

ACKNOWLEDGMENTS

Writing this thesis would not be possible without the help and support of great people in the Electrical Engineering Department and Nanofabrication Facility. I would like to thank Prof. Karl F. Böhringer, my thesis advisor and committee chair, for his guidance and support throughout my research. Equally, I would like to thank Prof. Rajashree Baskaran for her valuable advice and insights from the industry perspective.

I would also like to present my gratitude to the following people for their continuous help and support:

- Past and present members of the MEMS group, especially Bowen Cheng, Çağdaş Varel, Michael Wang and Kwang Soon Park, who have kept me in good company during my graduate studies.
- Past and present members of the Photonics Laboratory, especially Chang-Ching Tu.
- My parents, for always supporting me.

This work was supported by the Defense Advanced Research Projects Agency (DARPA) N/MEMS S&T Fundamentals program under grant no. N66001-10-1-4004 issued by the Space and Naval Warfare Systems Center Pacific (SPAWAR). Part of this work was conducted at the University of Washington Nanofabrication / Nanotechnology User Facility, a member of the NSF National Nanotechnology Infrastructure Network.

CHAPTER 1. INTRODUCTION

1.1 Introduction

The packaging and integration of microscale modules, such as sensors, actuators and transceivers, and data processing, microfluidic, power management, electromechanical and optoelectronic devices into heterogeneous multifunctional systems is one of the big challenges in the field of microelectromechanical systems (MEMS). The fabrication processes and the material prerequisites for the components are predominantly incompatible, thereby eliminating the possibility of fabricating them all on a common substrate, as it would have otherwise been done in a monolithic approach. Consequently, in a heterogeneous approach, the components of a system are fabricated separately under respective optimal conditions before being assembled to construct a functional system.

The prevailing method used for assembly and packaging in microelectronic manufacturing is robotic pick-and-place. This technique has proven accurate and reliable for large component scales, and its throughput is satisfying for consumer electronics applications [1]. However, pick-and-place is confronted with a trade-off between throughput and component placement accuracy. Furthermore, the method is serial, it requires closed-loop control and it becomes more expensive as device dimensions shrink, and registration constraints become more stringent. Furthermore, stiction problems [2] set in for device sizes smaller than 300 μm [1].

As the electronics industry nears the limits of historic CMOS scaling [3], prevailing growth driven by a continuous reduction in cost per function can no longer be sustained by the scaling of transistor density. The assembly and packaging sector is increasingly undertaking the responsibility of maintaining current growth rates, and it is doing so based on the principles of functional diversification and function densification. Functional diversification, also known as “More-than-Moore” (MtM) [4] focuses on system integration/heterogeneous integration rather than transistor density. Function densification, in the context of the prevalent planar fabrication processes, implies the use of stacking components to increase device density.

The intuitive concept of agitating a system and allowing pieces to fall into place is sometimes used in industry to address the stated problems; contemporary manifestations of this concept include the assembly of pin-grid and ball-grid arrays [5, 6]. As is obvious from the documentations of [5, 6], the term “self-assembly” is not found in the nomenclature, and it is still, largely, the case that stochastic processes are not recognized as an established methodology for component assembly in industry. Applications of stochastic assembly in industry are often one-off designs, meant to meet very specific assembly requirements, thus resulting in very limited understanding of the design-space and fundamental science. There exists no broader science base in this area, unlike in chemistry and physics (statistical mechanics), where typical processes are understood to be stochastic. Our group studies microscale self-assembly as a suite of techniques that augments both functional diversification and function densification motivated and refined by industry input. We demonstrate that self-assembly can not only improve existing assembly and packaging techniques, but also enable possibilities restricted by pick-and-place solutions currently used in industry.

1.2 Nomenclature

Even within the scope of microscale assembly and packaging, the term “self-assembly” is ill defined and has been liberally used. There are many works titled “self-assembly” that deal exclusively with alignment, rather than an entire assembly process. Notably, work from Koyanagi et al., though titled “self-assembly”, focuses on (and excels in) aligning and bonding silicon chips on micro-fabricated silicon pedestals of corresponding dimensions [7]. “Self-alignment” is probably a more appropriate title for such studies, drawing the distinction between investigations focused on alignment and work that also includes a stochastic transportation mechanism that brings discrete components to the vicinity of the intended assemblies.

Self-assembly has been defined as the autonomous organization of components into ordered patterns or structures without human intervention [8]. Specifically in the scope of microscale assembly and packaging, we add that: *self-assembly usually involves a stochastic transportation phase that brings discrete components to specified binding locations on a substrate, an alignment phase that correctly orients components at the binding sites, and a final step that permanently adheres components to the binding locations* [9] (Figure 1).

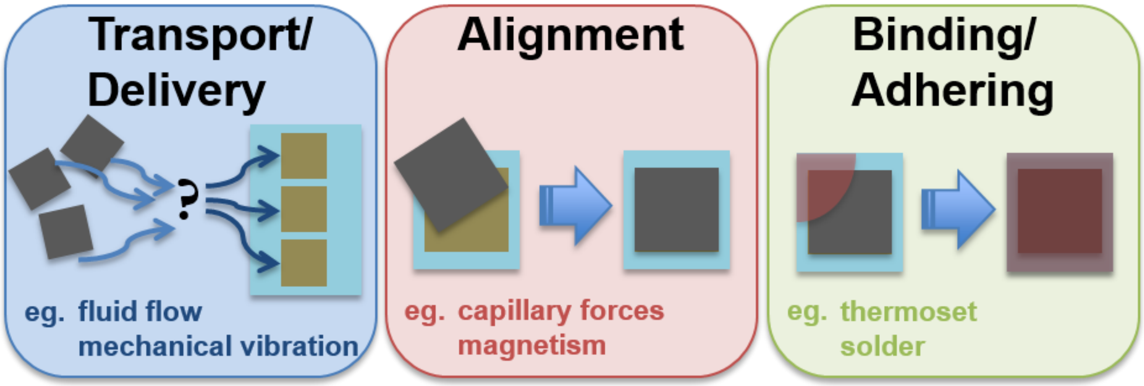

Figure 1. Self-assembly process can be separated into the transport, alignment and permanent binding/adhering phases. In the transport phase, components are brought to the immediate vicinity of binding/assembly sites; the alignment phase corrects the orientation of the component; the binding phase adheres the component onto the binding site permanently.

By this definition, works by Jacobs [10] and Parviz [11], are considered complete self-assembly processes, as they both use fluidic mediums to stochastically transport components to binding locations, employ molten solder to perform component alignment at said binding locations, and finally allow the solder to cool and solidify, thus mechanically and electrically adhering components to the substrate.

Finally, in the context of microscale self-assembly, “programmability” implies the ability to direct different reliably reproducible outcomes with the same set of components in a self-assembly process, as are demonstrated in works by Xiong [12] and Parviz [13].

1.3 Representative Works in Self-assembly

Microscale self-assembly methods can be broadly classified by their transportation and alignment mechanisms. Representative work within the field are listed in Table 1.

Table 1. Survey of current self-assembly processes. Components are square in shape except where marked by ^{C}, and ^{R}, which are circular and rectangular respectively. Part sizes of components are taken to be the length for square and rectangular parts, and the diameter for circular components.

Researcher, Institution	Assembly Mechanism					Part Size (lateral dim.) [µm]	Thickness [µm]	Aspect Ratio (lateral/ thickness)	Packing Density (in plane) [%]	Orientation Specificity	Reported Yield [%]
	Transport		Alignment								
	Fluidic	Mechanical Agitation	Shape Matching	Capillary Forces	Magnetic						
Yeh [14], Berkeley	√		√			**18**	**9.9**	**1.8**	**-**	**No**	**> 90**
Parviz [1, 11], UW	√		√	√		**100^{C}**	**10 - 20**	**5 - 10**	**20**	**Yes**	**97**
Srinivasan [15], Berkeley	√			√		**150 - 400**	**15 - 50**	**8 - 10**	**16**	**No**	**100**
Jacobs [10, 16], UMN/ Harvard	√			√		**20**	**10**	**2**	**25**	**No**	**> 98**
Böhringer [17, 18], UW	√			√		**1000 - 2000**	**100**	**10 - 20**	**25**	**No**	**100**
Böhringer [19, 20], UW	√			√	√	**2000**	**100**	**20**	**40**	**Yes**	**100**
Böhringer [21], UW		√	√	√		**370**	**150**	**2.47**	**80**	**No**	**100**
Böhringer [22], UW		√	√	√		**400^{R}**	**200**	**2**	**35**	**No**	**100**
Ramadan [23], IME		√	√		√	**1000^{C}**	**350**	**2.86**	**6**	**No**	**97**

1.3.1 Fluidic Transport – Shape Matching Alignment

Yeh et al. presented the seminal work based on fluidic transport and shape matching alignment [14], which later spun-off into a start-up. By combining Yeh's concept of shape matching under fluidic flow with capillary forces as drivers of self-assembly, Parviz et al. demonstrated the possibility to assemble multiple device types simultaneously onto a variety of substrates [1], including flexible plastics [11]. Based on similar delivery and alignment concepts, programmability was also demonstrated through the use of photosensitive materials to control the access of components to binding locations [13].

During the transportation phases of these self-assembly processes, components are flowed over substrates designed with traps that will only capture the components when the correct components approach the traps with the correct orientation. The traps act as an equal and opposite force against the gravitation pull on every component flowed over the substrates; the systems "error-corrects" by only permitting correct components/correctly oriented components to stay on specified locations on the substrate through the equilibrium of dynamic forces, and hence is a dynamic self-assembly process.

1.3.2 Fluidic Transport – Capillary Forces Alignment

Jacobs et al. demonstrated the use of fluidic transport and capillary force alignment for the assembly of LEDs and discrete monocrystalline solar cell chips onto flexible substrates [10, 16]. In the latter example, the delivery of components onto the destination substrate was performed by first confining the solar cell chips in a silicone-oil – water interface, and pulling the substrate through this interface in the proximity of the chips. This procedure allowed the solder-coated contact pads to come into contact with the chips, thereby aligning and assembling chips onto the contact pads [10].

Again, the dynamic interaction of forces, in this case, gravitation and capillary forces self-selects and self-corrects the placement (on the substrate) and orientation of chips onto the substrates during the transportation phase.

Parviz et al. has a very similar study in [24].

The self-assembly of very thin and fragile chips at an air-water interface [17-20, 25] is one of our group's competencies. Reference [19], in particular, demonstrates a degree of programmability, given that the presence, or absence, of magnetic force underneath particular binding sites effectively controls whether said sites would trap parts.

To bring components to the vicinity of the binding sites, the water medium which transports the components to the assembly templates is agitated. The templates are then withdrawn from the water, allowing the gravity to pull off excess components (from the surface of the template), allowing only properly placed components to stay on the template, held in place by capillary forces [17-20, 25]. This is another demonstration of a dynamic self-assembly transportation phase as previously defined.

1.3.3 Mechanical Agitation Transport – Shape Matching Alignment

Our laboratory previously demonstrated the use of mechanical agitation to distribute components in an air environment, and the use of shape matching to capture and align components [26]. In [27], our laboratory similarly uses shape matching to capture and align components, and also uses capillary forces to perform fine-alignment. Ramadan et al. extended the methodology by devising a methodology that uses magnetism in addition to shape matching [23].

The transportation phases of these assembly processes are also dynamic self-assembly in nature. We will discuss this in greater detail in CHAPTER 3.

1.4 Thesis Organization

The focus of this thesis work is concentrated on self-assembly processes based on the mechanical agitation transportation of micro-components. Initially, we were interested in methods to improve mechanical agitation transportation – shape-matching/capillary force alignment type process as presented in [27].

In CHAPTER 2, we document the study of ‘catalysts’ in the context of self-assembly processes. The presence of catalytic parts allows stochastic part-to-trap assemblies to be performed at lower accelerations than without, and thus allow said assemblies to be performed further from the acceleration-levels required to free trapped parts; this reduces the probability of part-disassembly, thus improving assembly yield. A model from chemical kinetics theory is adapted for the analysis of this catalyst-enhanced self-assembly process.

In CHAPTER 3, we document the study of a template-based self-assembly method previously introduced [27, 28]. The use of templates (separate from the substrate to be assembled upon) to guide the transportation and alignment of components is our approach to achieve the very high level of packing density which was required for the application of the assembly of a thermoelectric cooling (TEC) grid Table 1.

Using a modified actuator that introduces agitations that are in the plane of the assembly surface, unprecedented control of micropart-motion has been achieved; of note, components can be reliability induced into a “walking mode”, where components are moved across surfaces in predetermined directions with a surface-hugging behavior. Walking mode enables parts to be moved across surfaces and into binding sites, but do not cause trapped components to disassemble due to the suppression of out-of-plane agitation. Repeatable and programmable complete delivery of components into arrays of traps is achieved in open loop and feedback-enhanced configurations. The theoretical study of this template-based assembly method is performed with ($370 \times 370 \times 150\ \mu m^3$) test components, and walking modes are statistically characterized and a chemical kinetics inspired model is developed.

The above template-based self-assembly process is then applied on the assembly of 01005 (0.016” × 0.008”, 0.4 mm × 0.2 mm) surface mount technology (SMT) resistors and capacitors, demonstrating the (mechanical agitation) transportation, (shape matching/capillary forces driven) self-alignment, and adherence phases of our template-based assembly process.

In CHAPTER 4, we extend our self-assembly suite to the possibility of the assembly of said 01005 SMT components into through-wafer trenches with a vertical pose, by adapting the in-house visual-feedback systems used throughout the thesis work. Apart from all works previously introduced, the transportation phase of this work is largely magnetically driven, having been inspired by the similar delivery and assembly of ferromagnetic nickel through-silicon vias reported by Fischer et al. [29]. The process is benchmarked against theoretical upper bounds calculated for capacitors [30] and resistors fabricated through standard CMOS foundry processes, and found to be reasonably competitive.

CHAPTER 5 summarizes the work done thus far, and also details potential directions which could be pursued in the future.

CHAPTER 2. CATALYST-ENHANCED MICROSCALE SELF-ASSEMBLY

2.1 Introduction

Agitating a system and allowing pieces to fall into place is an intuitive concept, and has often been applied in industry in one form or another; contemporary manifestations include the assembly of pin-grid and ball-grid arrays [5, 6]. Our group has studied similar fully dry vibration-driven self-assembly methods in the micro scale [21, 22, 26-28]. For materials that may be sensitive to exposure to water or other liquid environments, these all-dry assembly methods offer a feasible alternative to fluidic assembly.

Batch assembly processes based on mechanical agitation (transportation phase) is a cost effective and fast alternative to pick-and-place robotics. In the assembly process presented here (example in Figure 2), microcomponents are delivered to microfabricated deep trenches using vibrations, analogous to [5, 6].

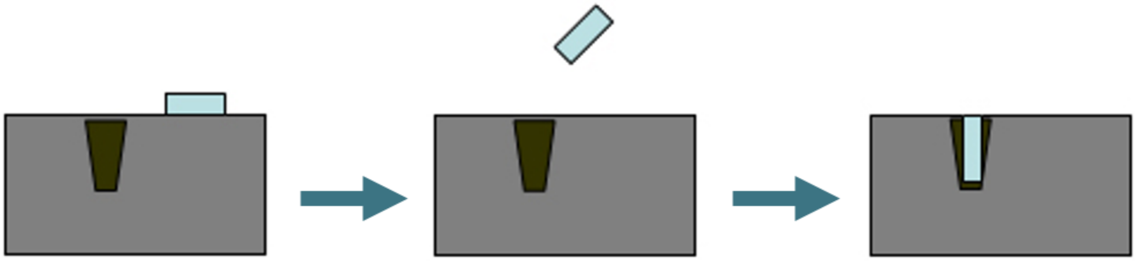

Figure 2. Representative mechanical agitation type process of delivering component into binding sites/apertures. Components initially placed on the substrate needs to be agitated to have the possibility of being caught in a binding site.

The vibration acceleration supplied should be high enough to keep the parts in motion (to facilitate the transportation phase) but lower than a critical threshold to keep the delivered parts in their traps. However, for part lateral size below 1 mm and thickness below 500 μm, surface forces (including van der Waals and electrostatic forces) are at least an order of magnitude stronger than gravity for silicon parts and highly dependent on ambient conditions (humidity and temperature). The acceleration necessary to free parts from their rest state (breaking free from stiction) from the surface of the substrate is often too close to the acceleration sufficient to allow delivered parts to escape their trap, thereby inducing dis-assemblies and preventing the system from achieving complete or near-complete part-to-trap delivery. An intuitive representation of this problem is shown in Figure 3.

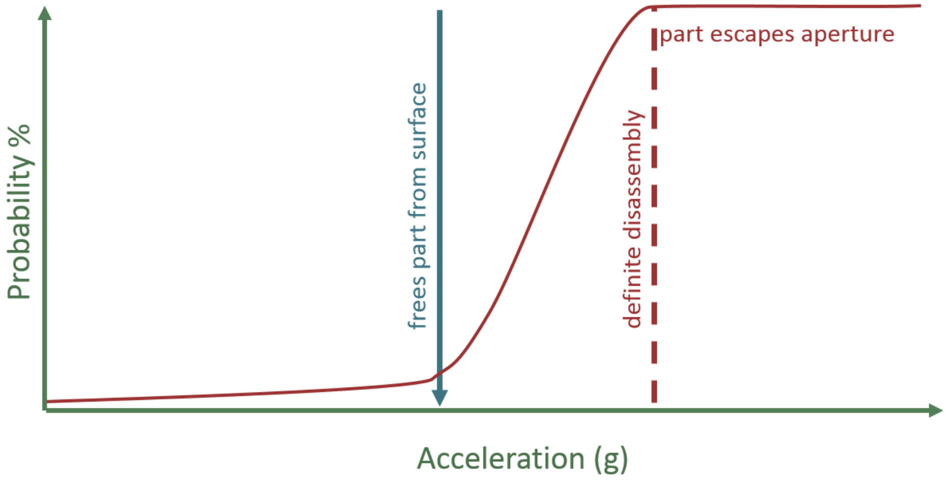

Figure 3. Graphic representation of dilemma for mechanical-agitation transported self-assembly process: The red curve indicates the probability that a component will escape from a binding site/aperture over a range of accelerations; the acceleration required to free components from surface and get them to start jumping often has a small probability of freeing captured components from traps.

.

Our interest to improve this process comes from the fact that template-based self-assembly processes previously presented [27, 28] were analogous to the depiction in Figure 2, with the exception that the traps were through-etched trenches on templates (to be elaborated upon in CHAPTER 3). We soon found that using non-participating ‘catalyst’ components, we can lower the acceleration required to start the stochastic transportation phase of the assembly process, allowing for the reliable delivery of all components.

2.2 Model Development

The modeling of microscale assembly processes using a chemical reaction analogy was introduced in [12]. The chemical analogy to our system is explained in Figure 4 and Table 2. We define 3 states for the parts: A, when the parts are outside of the assembly sites (initial state); A^*, when the parts are in free motion (activated); and B, when the parts are assembled onto the assembly sites (desired final state). The activation energy can be thought of as the height of the potential barrier that is separating two local minima of potential energy (of the reactants and of the products of reaction). In our case, the van der Waals and other surface forces are the source of this ‘energy barrier’.

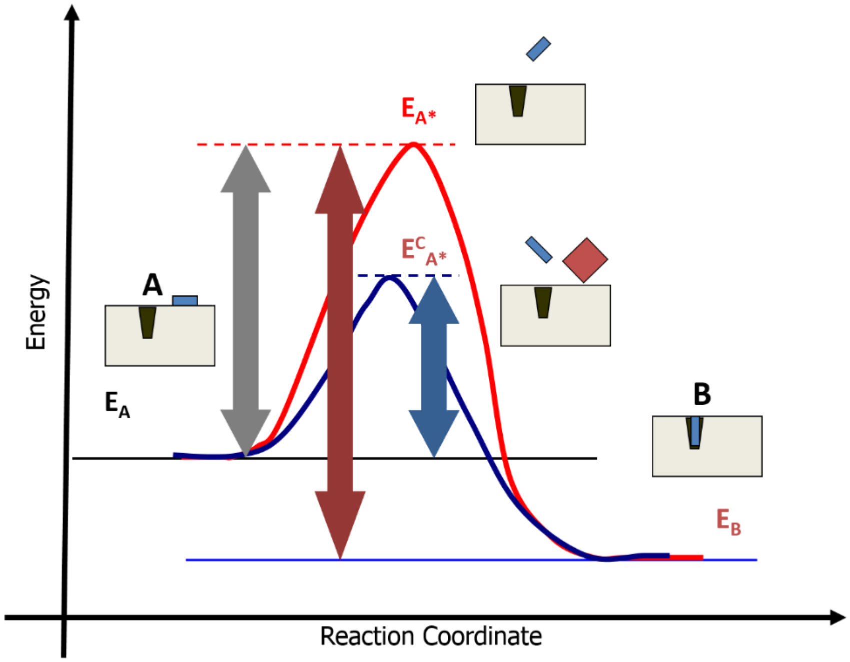

Figure 4. Schematic showing the average energy states for the assembly process A → B. The gray arrow represents the energy barrier without catalyst and the blue with catalyst. The red arrow shows the energy required for the reverse reaction B → A.

Table 2. Variables in the model of the batch assembly process that is developed in analogy to chemical reaction kinetics. Note that for the stage acceleration a and sinusoidal displacement amplitude x with frequency f, $a(t) = (2\pi f)^2 x(t)$.

Chemical reaction	Reactant	Products	Activated Reactant	Energy Barrier	Temperature
$A \rightarrow A^* \rightarrow B$	A	B	A^*	ΔE	T or a
Micropart dry assembly	parts outside the assembly site	parts inside the assembly traps	parts in air (parts jumping)	surface forces	stage acceleration

A catalyst functions by lowering the energy barrier of the reaction. In our dry assembly set-up, parts whose surface force to inertial force ratio is small can be triggered to move with smaller external acceleration. Once there is motion within the assembly area, many parts are triggered to move.

Another notion that is important in this context is that of concentration of reactants (total number of parts in a given surface area). In our particular case, the behavior of the parts under external agitation is also dependent on the concentration. When there is contact or adhesion between two parts at the initial state, the effective surface force of the combined part is different from that of the individual parts. As the concentration of the parts increases, the likelihood of parts stacked (and sticking) on others is high and their combined van der Waals force induced barrier is lower. Also, once one or a few parts start moving, they trigger other parts into motion; hence the barrier is a function of the distribution of individual parts on the surface and part-part interactions.

Typical dynamics of chemical reactions are modeled by differential equations that relate the rate of product formation and reactant consumption to concentrations of the reactants and products, and intermediate species. Note that for the case of systems with catalysts, the concentration of such catalyst species is also required to capture the correct dynamics. Typical reaction dynamics are described in equations such as the following one, where X and Y are the different reactant species.

$$Rate \equiv \frac{d[X]}{dt} = \kappa[X]^m[Y]^n \qquad (1)$$

The order of a reaction is defined as the sum of the powers m and n in Equation 1. The order for a chemical system with respect to each reactant is experimentally determined, which can be integer or non-integer, typically a value between –2 to 3. The negative values denote species that actively inhibit product formation [13]. The proportionality constant κ is called the rate coefficient and is independent of the concentration. For many elementary reactions, the number of reactants that are involved in a reaction step is also the order of the reaction. For reactions with catalytic activity, the concentration of the catalyst affects the reaction rate as well.

In our microscale system, it is difficult to estimate the overall order of our reaction. There are many elementary steps involved in the assembly process. All the possible elementary steps that were observed in our experiments for part activation are represented in Equation 2, where C is the catalyst. Even in the absence of catalysts, our system may behave in an autocatalytic fashion, i.e., an activated part 'hits' a stuck part and activates it. "AA" indicates two parts that are sticking to each other, distinct from "$2A^*$" where two parts are jumping independently.

$$\begin{aligned} &A \leftrightarrow A^* \\ &A^* + A \leftrightarrow 2A^* \\ &AA \leftrightarrow 2A^* \\ &A + C \leftrightarrow A^* + C \end{aligned} \tag{2}$$

The rate coefficient is typically a strong function of the temperature at which the reaction is occurring. In chemical reaction kinetics, the Arrhenius equation (Equation 3) states that the reaction rate coefficient κ depends on the ratio of activation energy ΔE and RT, where R is the gas constant and T the temperature. This implies that either an increase in acceleration a (our system 'T') or addition of catalysts, which reduces the energy barrier ΔE, must have the same effect of increasing κ.

$$\kappa \propto e^{\frac{-\Delta E}{RT}} \qquad (3)$$

In this study, we present experimental measurements of the energy barrier with and without catalysts. We also present experimental data on the rate at which parts are activated for the case of different reaction 'temperatures'. This rate of formation of A^* is directly dependent on the rate coefficient. The exact relationship of this dependence is a function of the order of the reaction.

2.3 Experiments

The experimental set-up and flow of data is shown in Figure 5. The parts ($800 \times 800 \times 50$ μm^3) and catalysts ($2 \times 2 \times 0.5$ mm^3) are made respectively from SOI/silicon wafers using standard microfabrication techniques. A polished silicon wafer is used as the assembly surface. To enable the observation of part motion due to vibration of the linear electromagnetic actuator (Brüel & Kjær Type 4809), we confine the parts using an optically transparent container. A high-speed camera is mounted to record the motion of the parts.

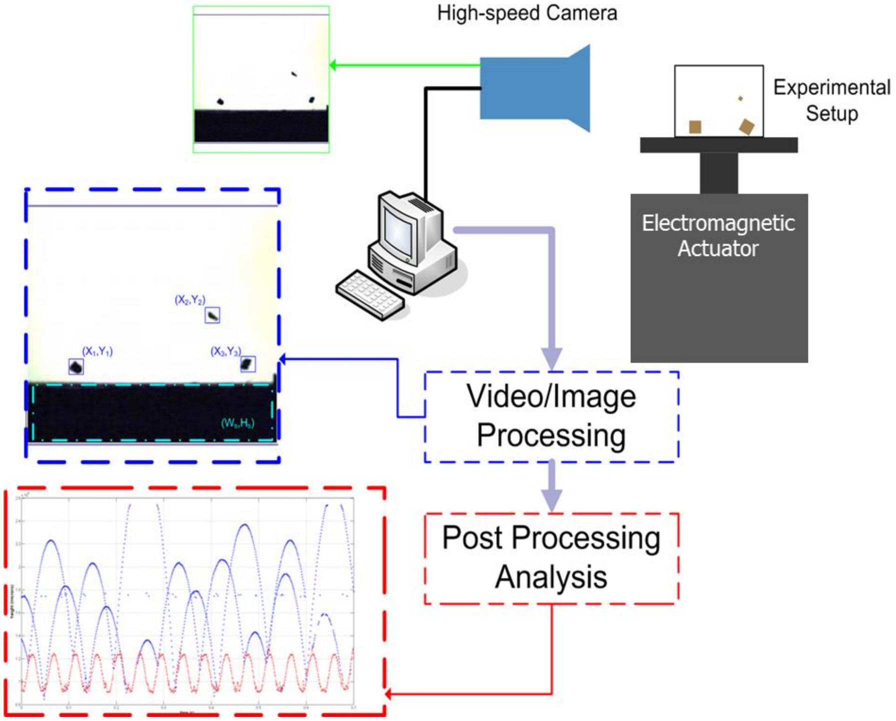

Figure 5. Schematic of the experimental set-up: An assembly area (2.5 cm wide, 10 cm tall and 1 cm deep) confines the parts on a microfabricated substrate, which is vibrated vertically using a LabView© controlled electromagnetic actuator. The high-speed video recordings are processed and analyzed using MatLab©.

Since the part motion dynamics happen in a time scale of milliseconds, the high-speed video recording and the subsequent image analysis are important tools for understanding the mechanism of part motion. For instance, Figure 6 shows data from a video segment that tracks part motion initiated in a case without catalysts, when 2 partially overlapping or ‘stuck’ parts are initially triggered to joint motion that then separate into 2 parts after the second impact with the assembly area surface (~1.05 s, indicated by an arrow in the figure).

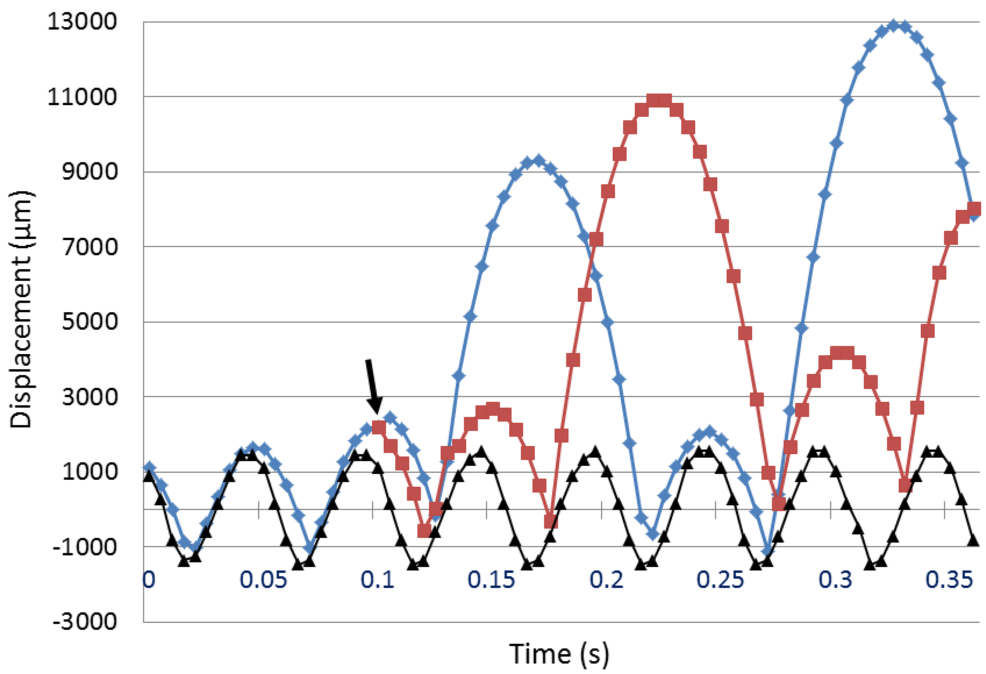

Figure 6. The vertical position of the surface (▲) and the center of mass of 2 parts (♦ and ■) that are initially 'stuck' (appearing as a single part) from image processing of a high-speed video. This is an example of $\boldsymbol{AA} \rightarrow \boldsymbol{2A^*}$*, verified with video.*

2.4 Results and Discussion

We perform a set of experiments to measure the energy barrier of our parts for different concentrations of parts, which is analogous to the concentration of the reactants in a chemical reaction. We start with an assembly area with the parts at no stage motion. We then ramp the acceleration of the stage in small steps of ~0.05 g. We note the instantaneous acceleration where the part starts to 'jump' and denote this as the minimum acceleration required to initiate part motion.

Figure 7 shows the minimum acceleration a required to initiate formation of $A*$ with and without catalysts for various initial part densities (proportion of substrate surface that is covered, at a rest-state, if no parts are overlapping; analogous to ‘concentration’); *a* is substantially reduced when a single catalyst is added. Also, note that there is little difference between additions of 1 or 3 catalysts. The standard deviation from the 5 experiments is very small for the case with the catalysts, compared to that without. These data also show that the presence of a catalyst is essential for any part motion below 10 g acceleration for low concentrations of parts.

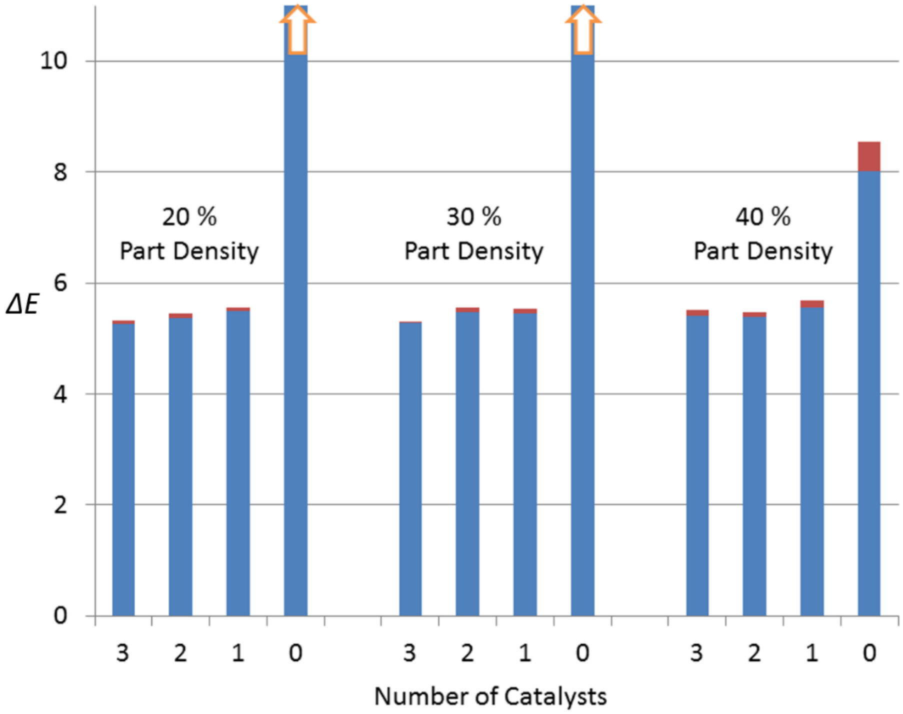

Figure 7. Energy barrier to formation of A from A: Minimum acceleration of the stage (number of g’s) at which parts start to jump. The values are averaged from 5 experiments with the standard deviations added in red. For 20% and 30% part densities, the accelerations required to move the parts were much larger than 10 g, and are widely distributed. On addition of a catalyst, micropart motion was consistently triggered at below 6 g.*

Our next set of experiments was aimed at measuring the rate of formation of *A** by addition of a catalyst at various ‘temperatures’ of our system. From the chemical reaction analogy, we expect from the Arrhenius equation that the addition of a catalyst must have the same effect on reaction coefficient as operating at a higher acceleration of the stage.

In order to measure the rates in which the parts were getting activated, we recorded videos starting at low stage acceleration (from 5 g), below the threshold for part motion. We increased the acceleration to various final values in one time step. From the image processing of the videos, we gather the data on individual part locations as a function of time. From this information, we can extract the data on total number of parts that are jumping (center of mass above a critical threshold value). In this plot, the real time axis is shifted such that $t = 0$ is the frame before the first frame at which at least one part jumped. All the videos were taken at the same frame rate of 1000 frames per second. Figure 8 shows the initial reaction rate for the case of $a = 10.6$ g with and without addition of catalyst. As expected, the reaction rate increases (~3×) in the presence of catalysts.

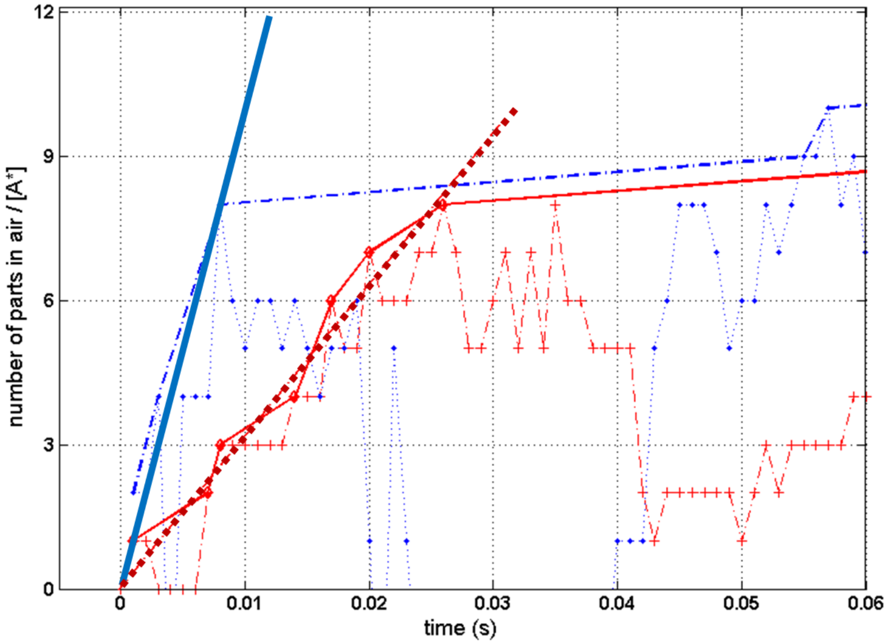

Figure 8. Initial rates of formation of A with (blue, 1000 #/s) and without (red, 300 #/s) catalyst for the case of 10.6 g: The time it takes for half of steady state A* to form,* $t_{1/2}$*, is ~0.01 s and ~0.02 s with and without catalyst, respectively.*

To measure the effect of a catalyst on the assembly process, we studied its influence on assembly rates in comparison with an increase of the stage acceleration. If the parts can be activated using catalysts instead of using higher stage acceleration, assembly can be achieved at lower ‘temperature’ of the system. This is a vital aspect of the assembly process as this would potentially enable good part-delivery/assembly yields since we can operate at energies below the level at which the parts will be triggered out of the traps.

Figure 9 shows experimental results of the rates of formation of $A*$ at different values of acceleration. As a increases from 9 g to 12.7 g, without catalysts, the total number of activated parts increases from 3 to 23. In this case, the total number of parts in the assembly box was 30. But with the addition of 3 catalysts, the total number of parts in air for the case of 9 g was increased 5 fold. At higher accelerations however, there is diminishing return on addition of catalysts. At 12.7 g, there is no noticeable increase in total number of parts in air.

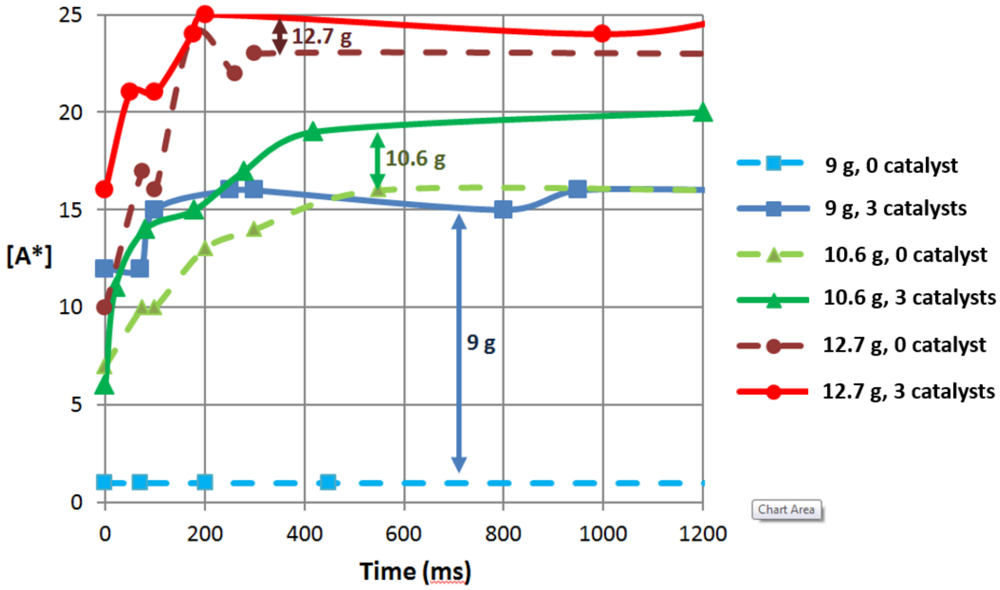

Figure 9. Experimental measurement of concentration of parts in air, A, with catalyst (solid-line) and without catalyst (dashed-line), for 30 % part density, at various accelerations a. The benefit for the addition of catalysts is most significant at low a values; in the case of 9 g, catalysts are crucial in the activation of the parts.*

Finally, we introduce a catalyst part ($2 \times 2 \times 0.5$ mm^3) into a set-up previously introduced in [27]. The objective of the experiment is to deliver parts ($370 \times 370 \times 150$ µm^3) into every trench on the assembly surface, such that trapped parts are standing on their sides within each trench, in preparation for the next assembly step [27]. The value of *a* required to kick-start parts at rest into motion is at an average of 4.0 g, while the *a* required for an experiment with a catalyst averages at 2.9 g. Figure 10 i and ii show a catalyst set into jumping motion, and subsequently agitating the smaller parts.

The presence of a catalyst allows part motion (and hence delivery) to be initiated at a lower a, which is further from the average value required to allow an assembled part to escape from its trap (about 5.1 g in this set-up). Assembly experiments, without a catalyst, conducted with an agitation of 4.0 g have an average of 89.6 % (σ = 2.22 %) completeness after 3 minutes of agitation. Experiments with a catalyst, conducted at an agitation of 2.9 g, have an average completeness of 98.1 % (σ = 1.52 %) after 3 minutes. Figure 10 iii shows an instance of a complete assembly enabled by the presence of a catalyst.

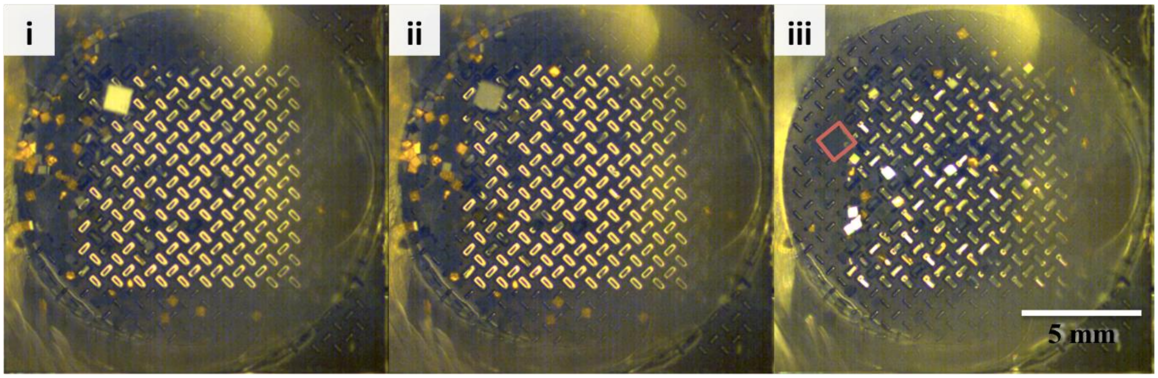

Figure 10. Catalyst-enhanced micro-part delivery: (i) and (ii) shows catalyst kick-starting part motion and, hence, assembly (bright rings are empty traps); (iii) shows completed assembly of parts into traps. The catalyst is outlined in red.

2.5 Conclusion

We present experimental evidence to support a new concept of catalyst-enhanced microscale assembly. Catalytic components enable stochastic micropart assemblies to be performed at energy levels lower than in cases without them, and thus allow assembly operations to be performed further from energy levels that would cause the disassembly of trapped parts – ultimately improving assembly completeness. The method could offer pathways for development and realization of an efficient, economical alternative, or supplement, to pick-and-place robotics. We also present an analytical framework inspired from chemical kinetics that can sufficiently explain the experimental data obtained.

CHAPTER 3. TEMPLATE-BASED SELF-ASSEMBLY FOR MICROCOMPONENTS

3.1 Template-based Self-assembly

Proximate active cooling solutions are increasingly sought as the industry achieves diversification and densification goals by applying methods such as system in package (SiP). SiP processes electrically and mechanically integrate dies from disparate processes into a functional package. The increased (three dimensional) device density strains prevailing package thermal management regimes.

Our template-based self-assembly technique was developed around the desire to assemble dense grids of next-generation thermo-electric cooling (TEC) chips in the immediate vicinity (on the devices, within the organic package) of thermal hot spots. Active cooling at hot spots works to redistribute concentrated heat, and thus permits the improvement of the form-factor of device/package-wide heat-dissipation solutions. Other benefits include the possibility to implement energy efficient feedback driven cooling schemes.

The p-type and n-type TEC chips (independently developed by Intel Corp.) are expected to be 100 – 500 µm in lateral size, and about 100 µm in thickness. The required surface coverage of these components is 80% of the substrate surface or better.

Since an earlier publication on the subject [27], the template-based self-assembly process has developed through several iterations. The latest process-flow is as follows in Figure 11 (silicon test parts have one side coated with gold; all gold surfaces are treated to be hydrophobic using dodecanethiol self-assembled monolayers (SAM)).

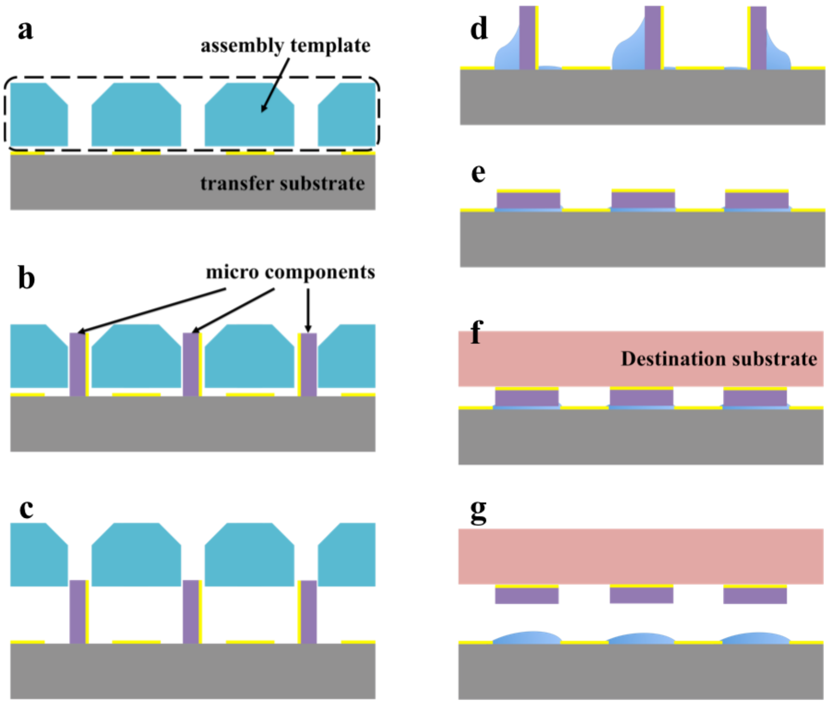

Figure 11. Assembly process flow: ***a****. mount assembly template on a gold patterned transfer substrate;* ***b****. assemble parts;* ***c****. remove template;* ***d****. apply moisture;* ***e****. vibrate setup gently to have parts fall on hydrophilic side and self-align;* ***f****. attach parts to destination substrate/device;* ***g****. complete process by removing assembled substrate/device from transfer template.*

Each run of the process shown in Figure 11 completes half the grid (Figure 12b, Figure 12e). In the case of the assembly of discrete TEC devices, we can assemble p-type components, onto a prepared substrate, in the first pass, n-type components on the second pass, and lastly, lay the final connections required to make the TEC grid functional (Figure 12).

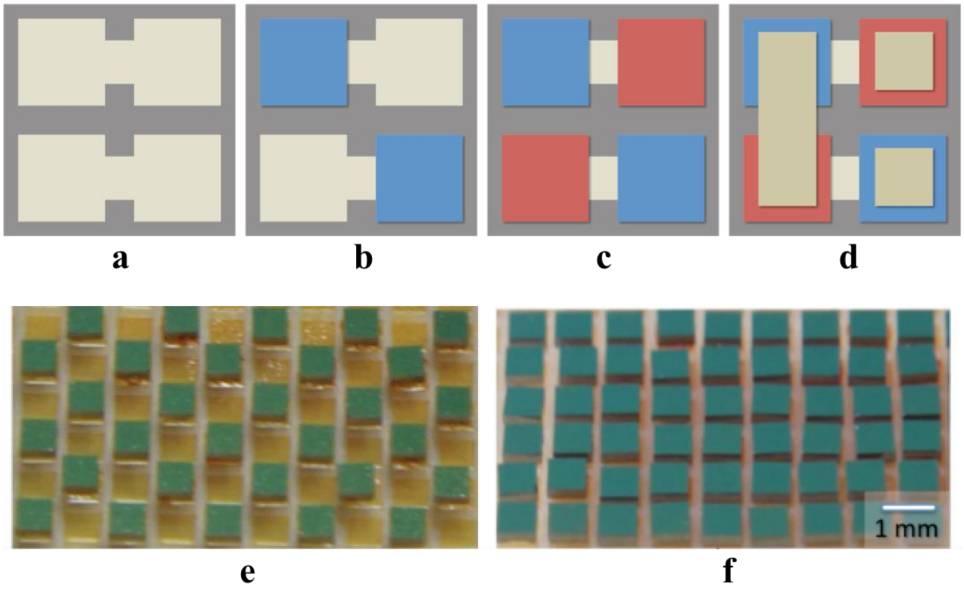

*Figure 12. Assembly schematic of TEC grid (**a**, **b**, **c** and **d**): **a**. substrate with contact pads and connections; **b**. assembly of p-type TEC chips; **c**. assembly of n-type TEC chips; **d**. final connections to make TEC grid functional (squares on the two chips on the right are contact pads). Test chips (790 × 790 × 330 μm^3) used to create grid of chips (**e**, **f**): **e**. picture after first pass (chips are held in place using photoresist); **f**. picture after second assembly pass (**e** and **f** are reprinted from [27]**)**.*

Through experimental analysis we discovered that the performance bottleneck on mechanical agitation type self-assembly processes is the tendency of components to escape from the apertures in the assembly templates [27]. The vertical agitation (perpendicular to the substrate plane) used to distribute and transport components over the assembly area has a sizable likelihood to impart enough energy for delivered components to jump out of the traps [31] (CHAPTER 2); incomplete assemblies were predominantly caused by escaping parts during the delivery process.

To mitigate this problem, we employed a modified linear electromagnetic vertical vibration table (Brüel & Kjær Type 4809) which can generate planar displacements perpendicular to the vertical actuation [21] (Figure 13). We identified three types of component motions, which can be induced with this setup, in Table 3.

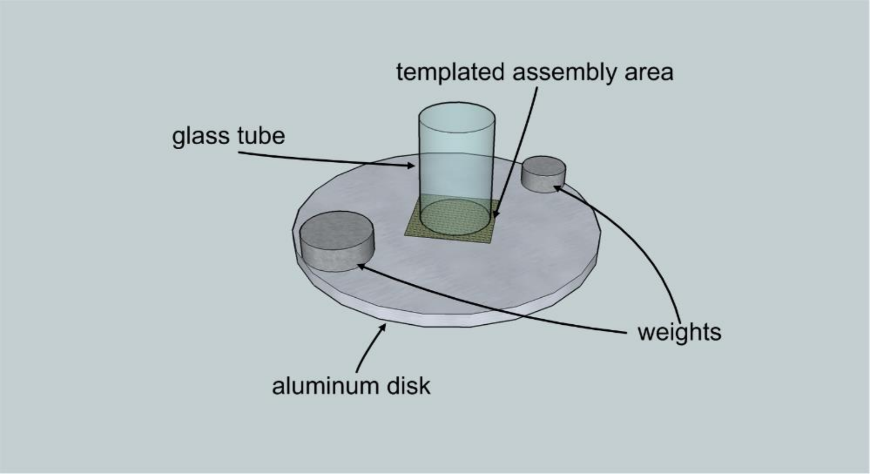

Figure 13. Weight-biased aluminum disk. Ordinarily, there will not be weights set upon the aluminum disk, which is mounted onto a Brüel & Kjær Type 4809 linear electromagnetic actuator. The presence of the 'unbalanced' weights imparts part of the vertical actuation into in-plane agitation, relative to the surface of the disk/template assembly area, and the net effect on component motion varies considerably with component size, frequencies of the signal input to the actuator, and other factors.

Table 3. Micro-component Motion Modes

Mode	**Description**	**Side-view**
Stationary	High-frequency perturbation of components to prevent/undo stiction between parts and template; does not disturb assembled components	
Jumping	Directional/random rapid part motion which can remove delivered components from traps	
Walking	Directional "surface-hugging" part motion which does not perturb trapped components; free parts can travel over filled traps	

The modifications to the vertical vibration table couples part of the vertical agitation into planar displacements, thus allowing silicon test parts modeling the dimensions of projected TEC components (370 × 370 × 150 μm^3) to be moved across silicon surfaces. By changing the frequency and amplitude of the driving signal that is supplied to the modified vibration table, we are able to control the movement of components on an assembly template or substrate with random jumping, directed jumping, and directed walking modes (where components move across the surface in the defined direction with a surface-hugging behavior resembling crawling or walking) with LabVIEW programs. Stationary modes are used to “prime” the system, imparting energy, enabling parts to more easily overcome stiction in walking or jumping modes. Using a laser vibrometer, we are able to extract the precise agitations of the vibration table which induces the various motion modes. The motion of the vibration table which induces a jumping mode motion is shown in Figure 14.

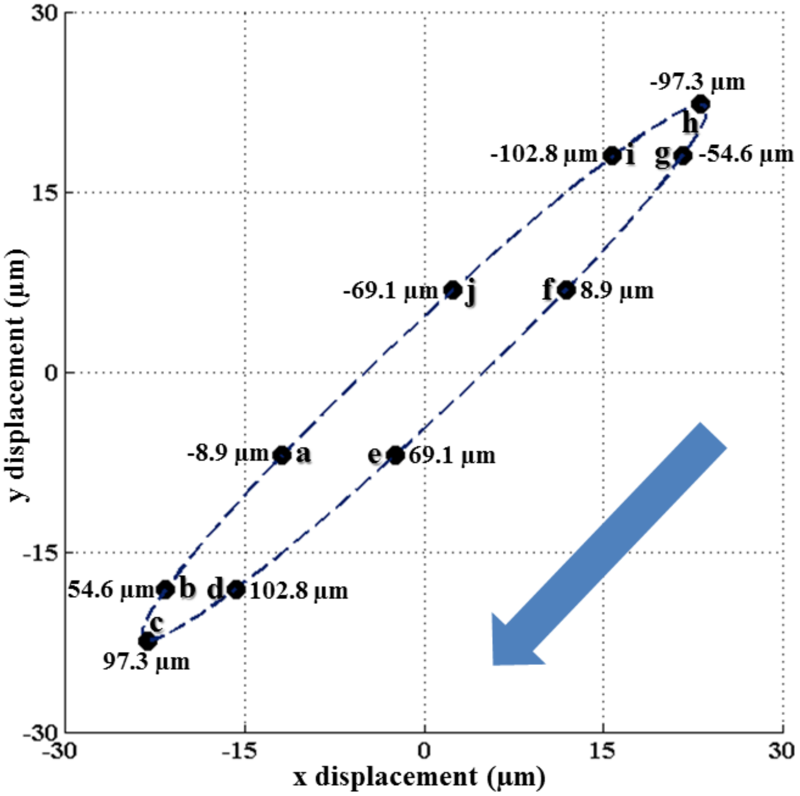

Figure 14. Agitation which induces 2 cm/s jumping mode behavior with 370 × 370 × 150 µm^3 silicon components on polished silicon surfaces in the direction as indicated by the blue arrow. a, b, c, d, e, f, g, h, i, and j indicate the positions of a point on the vibration table at time 0 s, 0.67 ms, 1.33 ms, 2.00 ms, 2.67 ms, 3.33 ms, 4.00 ms, 5.33 ms, 6.00 ms, and 6.67 ms, respectively; lengths accompanying each point indicate the out-of-plane (z axis) displacement at each instance.

The significance of the walking modes is the ability to move components across assembly areas without disturbing components that are already delivered into traps. Delivery processes can also be made to be feedback driven, where visual feedback is used to identify empty apertures and direct excess components towards them, guaranteeing complete delivery. Similarly, when all traps have been filled, excess components can be transported away from assembly areas to be collected.

We compare the displacements of the modified vibration table which induce a jumping mode behavior and a walking mode behavior in our components, in the same direction in Figure 16.

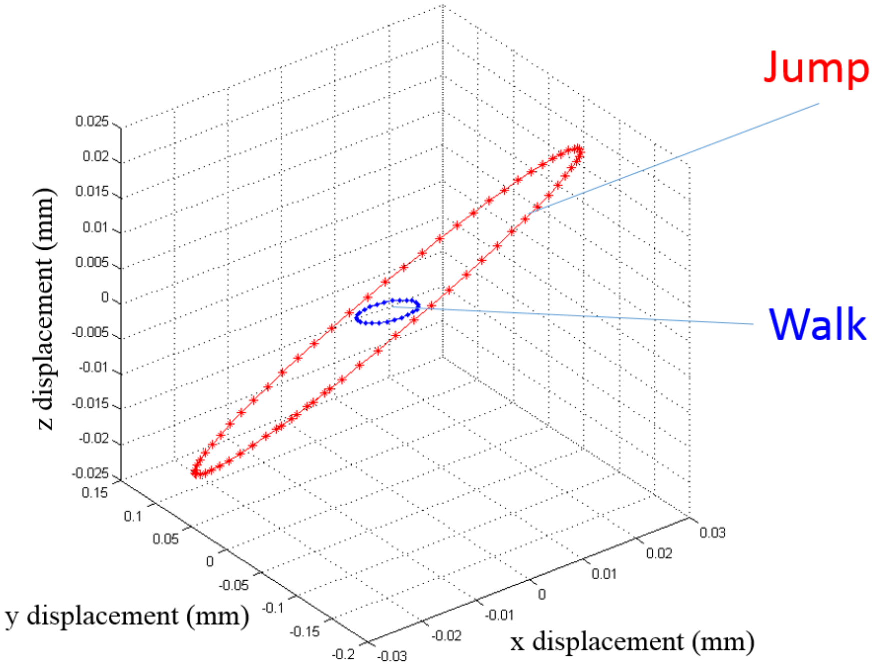

Figure 15. Comparison the displacement of the modified vibration table when it causes 370 × 370 × 150 µm^3 components to perform a walking mode and jumping mode behavior in the same direction.

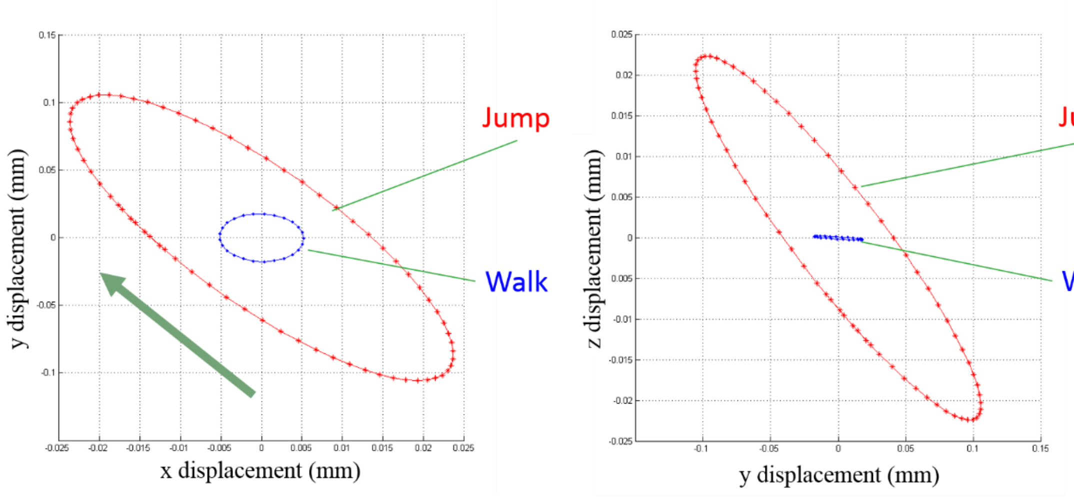

Figure 16. XY and YZ view of three-dimensional trace of the displacement of the vibration table in Figure 15. Approximate direction of part movement is indicated by the green arrow in the left-side graph.

To describe the generation of part motions independent of the specificity of our modified linear electromagnetic vertical vibration table, we documented the parameters required to generate various motion modes using our 370 × 370 × 150 μm^3 components on our assembly templates as shown in Table 4.

Table 4. Parameters for generating the various part motions, derived from a particular modified vertical actuator configuration; relative directions are specified in Figure 17.

Setting	Frequency	Mode	Direction	z amplitude	Phase-shift	y amplitude	Phase-shift	x amplitude	Phase-shift
				µm	radians	µm	radians	µm	radians
1	150	Jump	C	157.46	0.77	22.39	0.30	23.66	0.83
2	180	Jump	B	111.85	0.84	24.40	0.47	43.33	0.98
3	200	Jump	A	38.20	0.89	7.16	0.46	35.01	0.14
4	300	Walk	A	15.12	0.70	3.13	0.11	6.37	0.37
5	400	Walk	C	12.45	0.73	1.39	0.38	3.94	0.55
6	400	Walk	C	14.40	0.73	1.35	0.39	4.46	0.54
7	400	Walk	C	16.43	0.73	0.24	0.39	5.21	0.54
8	500	Walk	D	13.45	0.63	1.03	0.40	2.45	0.67

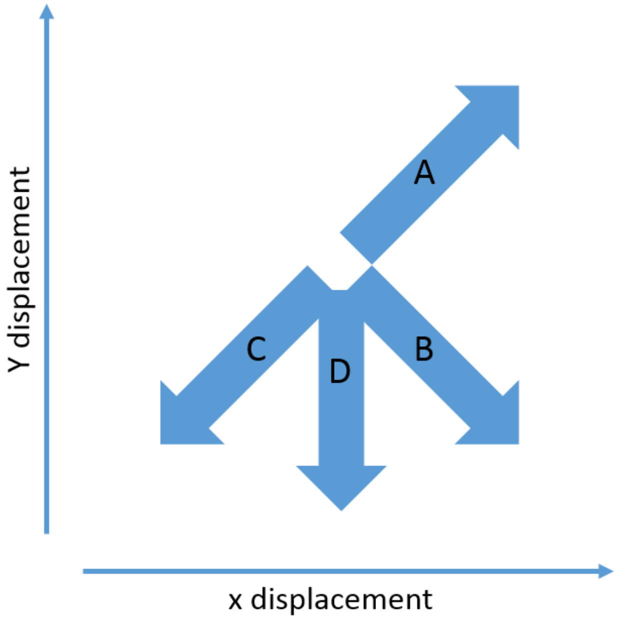

Figure 17. Directions A, B and C as specified in Table 4. Directions are relative to x and y displacements as measured by a laser vibrometer.

Settings 5, 6, and 7 in Table 4 are three walking mode settings driven with the same frequency input, to the vibration table, but at different voltage-amplitudes, translated into difference in z displacement amplitudes. The increase in z amplitude increases the walking speed of the components, up to a point when walking mode cannot be properly maintained (due to the ejection of trapped components due to the increase in z displacement). Settings 5, 6, and 7, walk $370 \times 370 \times 150\ \mu m^3$ components at approximately 0.10, 0.12, and 0.13 cms^{-1} respectively.

Given a "universal actuator" which can generate any form of actuation, one may reproduce motion modes by inserting parameters from Table 4 into the following equation for x displacement:

$$x(t) = X \cdot \sin(\omega t + \varphi) \tag{4}$$

where $x(t)$ is the x displacement, X is "x amplitude" from Table 4, ω is $2\pi \times$ Frequency (Table 4), and φ is the Phase-shift in radians from Table 4. The corresponding displacements required for the y and z (vertical) axes can be similarly derived from equation (4) and the relevant values from Table 4.

As previously mentioned, our template-based self-assembly process is a dynamic self-assembly process as defined by Whitesides [9]. In the walking mode delivery processes, each aperture in our template traps a single part, and holds it in place, against the planar force imparted by the walking mode delivery process. The presence of the template inhibits the planar force from displacing trapped parts, but allows excess components to continue to be transported over the template.

3.1.1 Design and Fabrication

To test our component transportation method, we designed a 200-slot assembly template for our silicon test parts based on the surface coverage requirements of the stipulated TEC grid previously described. Assembly templates are fabricated using silicon wafers. The design of the traps for our silicon test parts ($370 \times 370 \times 150\ \mu m^3$) is based on design rules specified in [27]. As shown in Figure 18, we also chamfered (timed KOH or HNA etch) the openings of each trap, increasing the effective capture area of each trap without sacrificing component coverage density coverage density [27].

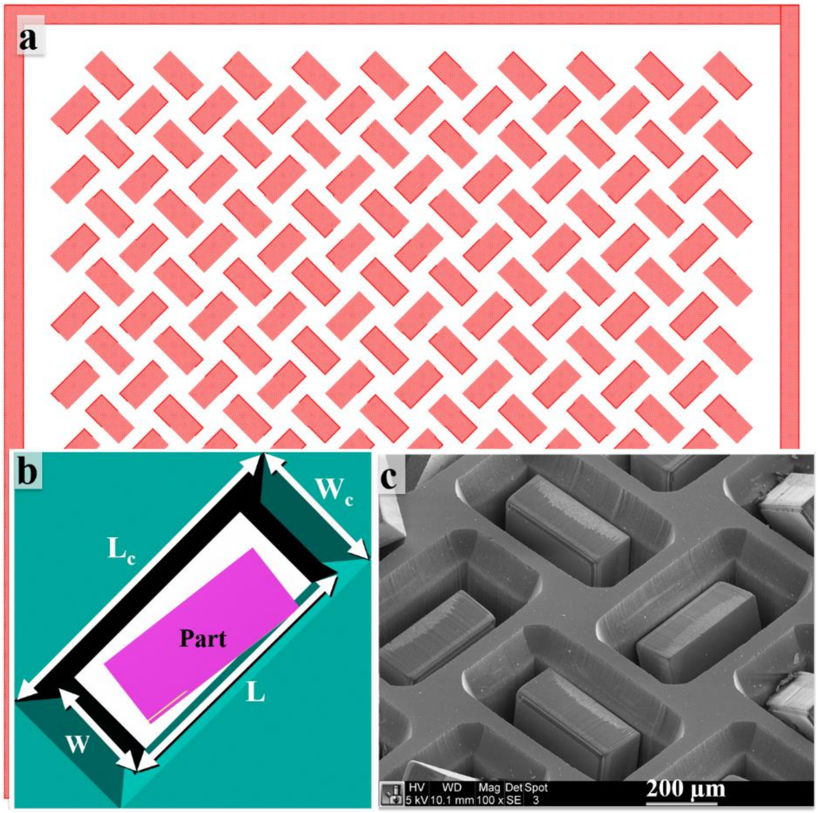

Figure 18. ***a****: layout of 200-slot assembly template.* ***b****: top-down view of a model of a single silicon part standing in a trap/aperture. Original trap-opening size: 530 (L) × 250 (W) µm. Size of effective trap-opening (after chamfering): 620 (L_c) × 300 (W_c) µm. b: SEM picture of silicon parts in traps with chamfered openings.*

While silicon test components and the target substrate shown in Figure 11 are made with standard microfabrication techniques, the fabrication of the assembly templates with chamfered openings is noteworthy (Figure 19).

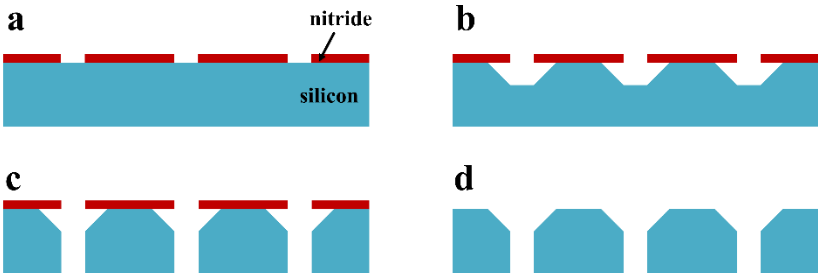

Figure 19. Fabrication process of chamfered templates. ***a****. a nitride layer is first deposited onto the silicon wafer surface, and openings, corresponding to the locations of apertures, are made with an RIE process;* ***b****. undercut rings are made at each opening using timed KOH or HNA etch (both methods attempted, both results satisfactory);* ***c****. using the nitride layer as a mask, through etch is performed with a DRIE process;* ***d****. completed template.*

Both isotropic HNA (HF, Nitric Acid, and Acetic Acid) and anisotropic KOH etch were attempted in the fabrication of the chamfered aperture openings. The rounded and polygonal openings, respectively, were functionally identical.

3.1.2 Walking Mode Delivery Experiments

Figure 20 shows the delivery of silicon test components into an assembly template of 200 traps, guided using visual feedback. Unoccupied traps can be visually identified as white oval rings (Figure 20a). MatLab® routines have been developed to capture the entire delivery process, keeping track of free components, empty and filled traps, and can be expanded to automatically guide the process towards complete delivery.

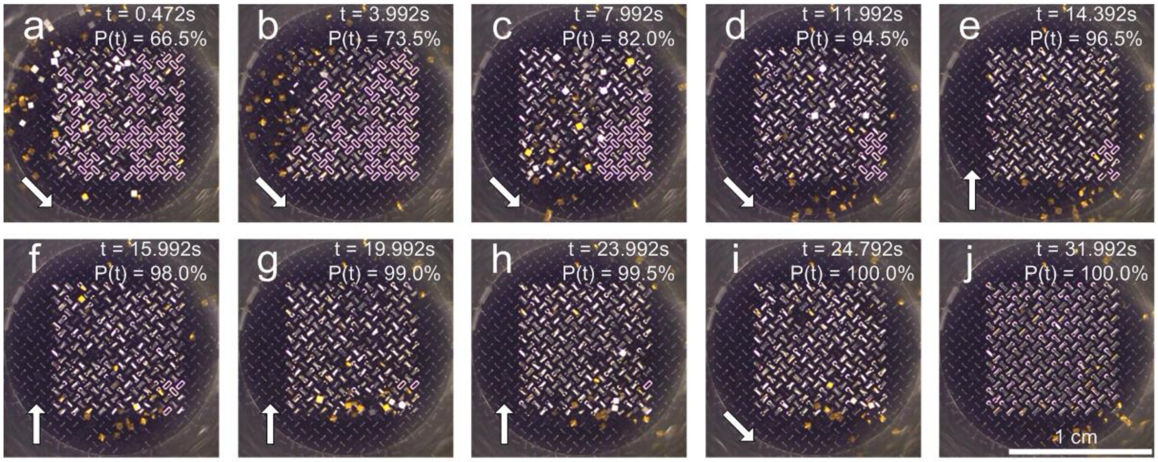

Figure 20. Stages of a feedback driven transport of 370 × 370 × 150 µm^3 components: ***a*** *shows the instance when we switch from jumping mode (with a top-left corner bias) to a walking mode with part-motion direction as indicated by the white arrow in the box.* ***b****, and* ***c*** *show the progressive filling of the entire assembly area (bright oval rings are empty traps). Right after* ***c****, when delivery-percentage, P(t), has plateaued, we activate a walking mode in the upwards direction as seen in* ***d****,* ***e****,* ***f****,* ***g****, and* ***h****, moving excess parts, aggregated below the assembly area, to the empty sites. After achieving 100% delivery in* ***i****, we switch to a walking mode towards the lower-right corner, moving excess parts away from the assembly area, finishing the process in* ***j****. Note: size-scale is provided in image* ***j****.*

The programmability of our methodology is partially demonstrated in the feedback driven transportation phase. Given any template with two separate regions of binding sites, we will be able to direct parts to either region (or both regions) repeatedly and predictably, thereby enabling distinct outcomes without any change in components.

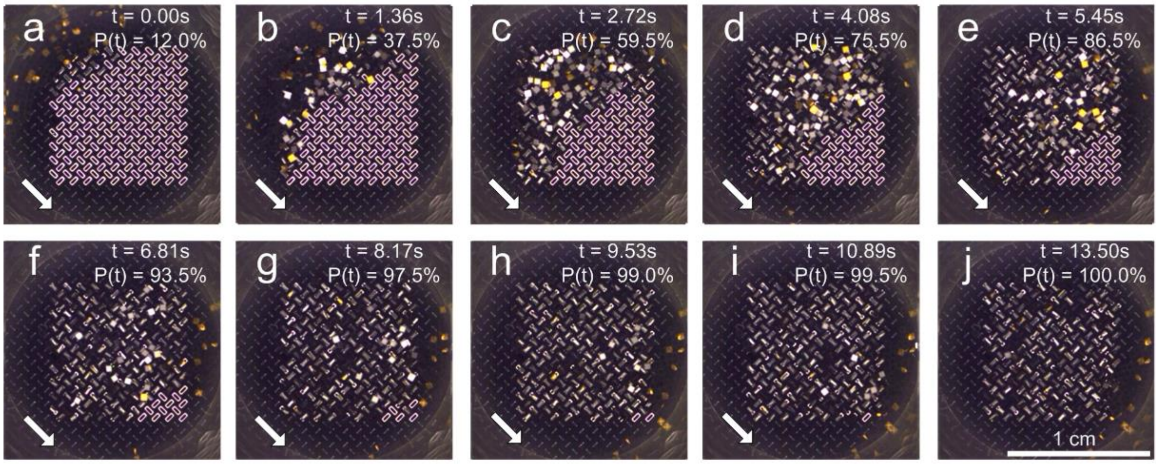

Figure 21. Stages of a non-feedback driven transport of 370 × 370 × 150 μm^3 components: ***a*** *through* ***i*** *shows the transportation of components across the 200-trap assembly area in the same direction with 50% part redundancy. Note: size-scale is provided in image* ***j****.*

A non-feedback driven delivery of components into 200 traps is shown in Figure 21. For non-feedback driven delivery of parts, we envision walking parts according to a predetermined sequence that, given a certain amount of excess parts, effectively nullifies the possibility that any slot could be left empty after the run.

3.1.3 Model of Walking Mode Delivery Process

We revisit the chemical kinetics rate equation to describe our system.

$$r = \frac{d[E]}{dt} = -k[P][E] \qquad (5)$$

Where r is the rate of change of empty aperture sites, $[E]$ is the number of empty aperture sites, and $[P]$ is the number of free parts. We observe, during our experiments, that the number of excess components do not affect the rate in a significant way. Hence, a pseudo first-order equation below will sufficiently describe our system [32].

$$r \approx -k'[E] \qquad (6)$$

And, thus:

$$E = E_o e^{-kt} \qquad (7)$$

Given that we are interested in the proportion of filled aperture sites over time, we write:

$$P(t) = A(1 - e^{-kt}) + B \qquad (8)$$

Where P is the percentage of filled aperture sites, A is the percentage of empty apertures, and B is the percentage of filled apertures at the beginning ($t = 0$). Since we are dealing with proportions, the sum of A and B is less than or equal to 100%.

The reaction rate constant k is a function of drive frequency and displacement of the sinusoidal signal supplied to the vibration table. Using different input conditions, we experimentally obtain the equivalent rate constants by performing analysis on high-speed video recordings of our experiments, and fitting equation (8). Figure 22 shows image analysis results from videos of two instances of our assembly process (all other experimental parameters held constant except driving frequency of the actuator) on the assembly template shown in Figure 21 with 50% part redundancy.

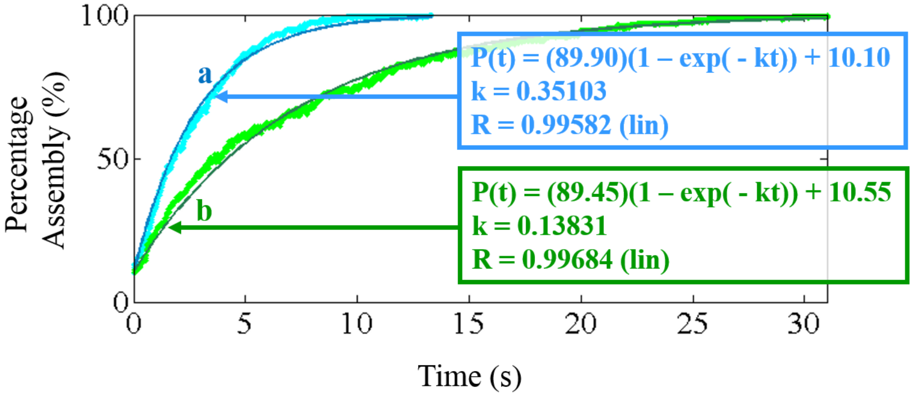

Figure 22. Image analysis results from two 125 fps videos of our assembly process, driven by a. 525 Hz and b. 565 Hz, actuator calibrated to output 4.65 g at 100 Hz, with 50% part redundancy. Our model is fitted into each set of data points to obtain the values for our rate constants k. Constants of each equation accounts for delivery that occurred prior to commencement of experiment.

From Figure 22, we see that our model fits the data very well. We then ran many walking mode delivery sequences at four different frequencies (505 Hz, 525 Hz, 545 Hz, and 565 Hz) while maintaining all other input parameters. The curve-fitting of data from four experiments performed at 545 Hz is shown in Figure 23, showing consistently good fits.

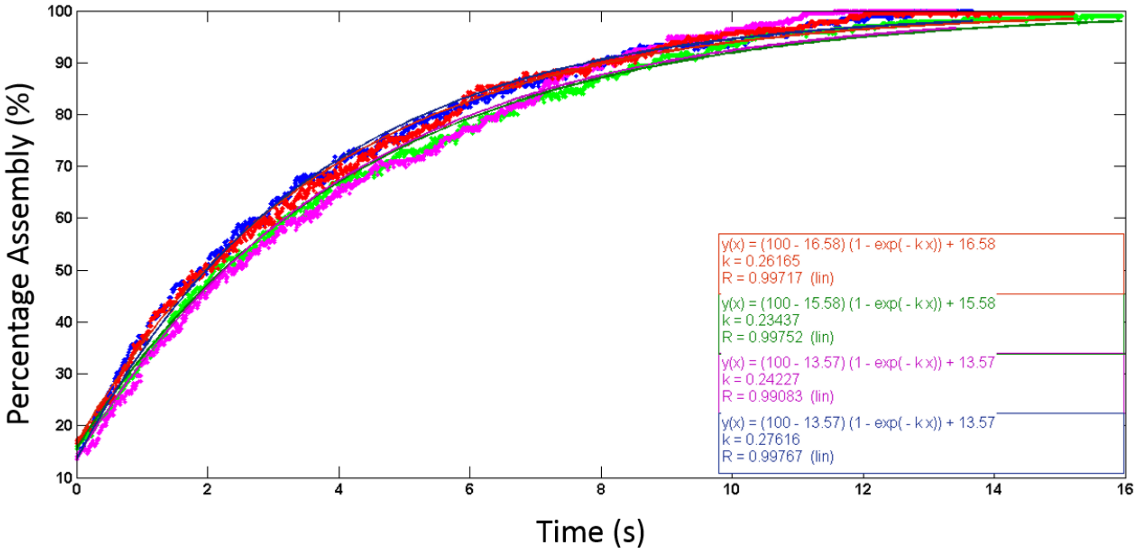

Figure 23. Curve-fitting of data from four walking mode deliveries to a 200 aperture template performed at 545 Hz with 50% part redundancy. The voltage setting of the actuator is calibrated so as to output 4.65 g at 100 Hz (a standard throughout our experiments).

Figure 24 shows the averages and variances of *k* for different drive frequencies, derived from five experiments at each frequency.

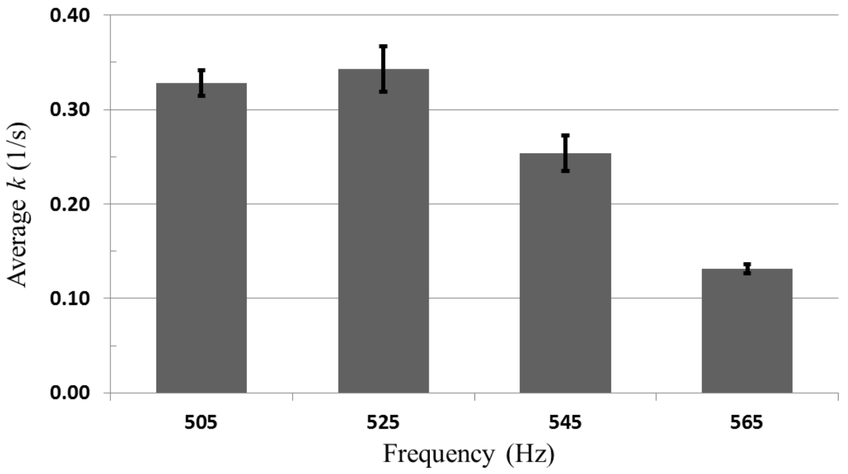

Figure 24. Averages of rate constant (k) for different drive frequencies, 5 experiments each, at actuator inputs calibrated to put out 4.65 g at 100 Hz vibration, with part redundancy of 50%.

Error bars indicate standard deviations.

Results reported in Figure 22 and Figure 24 allow us to engineer reliable open-loop/non-feedback delivery sequences.

Each batch of template-based assembly for our 790 × 790 × 330 μm^3 test chips covers 31% of the target substrate, providing a total surface coverage of 62% with two transfers (Figure 12 [27]). With two transfers, our 370 × 370 × 150 μm^3 test parts will bring total surface coverage up to 80%, achieving our stipulated goal.

The rate of assembly can be tuned with the system input parameters effectively, thereby giving us a window of process parameters to work with for different part sizes and/or assembly areas. Also the tight distribution of the assembly rates, even within a laboratory setting, demonstrates that the process is robust and repeatable.

3.1.4 General Model for Walking Mode Delivery

Although reliable, the model described in 3.1.3 is specific to instances of our walking mode assembly, where components are introduced into a square-shaped assembly area from a corner, as shown in 3.1.3.

We observe that components are reliably delivered into apertures at the front of the ‘wave’ of components that is driven across the assembly area during walking mode; the wave front of components delivers components into apertures in the vicinity, and continues to move in the prescribed direction of the walking mode, traversing said apertures. Furthermore, delivered components are extremely unlikely to be ejected from the apertures upon delivery.

We can hence assert that (assuming an abundance of excess parts):

The total number of components successfully delivered to an assembly area is the number of apertures that has been traversed by the wave of components.

For instance, assume that we had an assembly area as depicted in Figure 25.

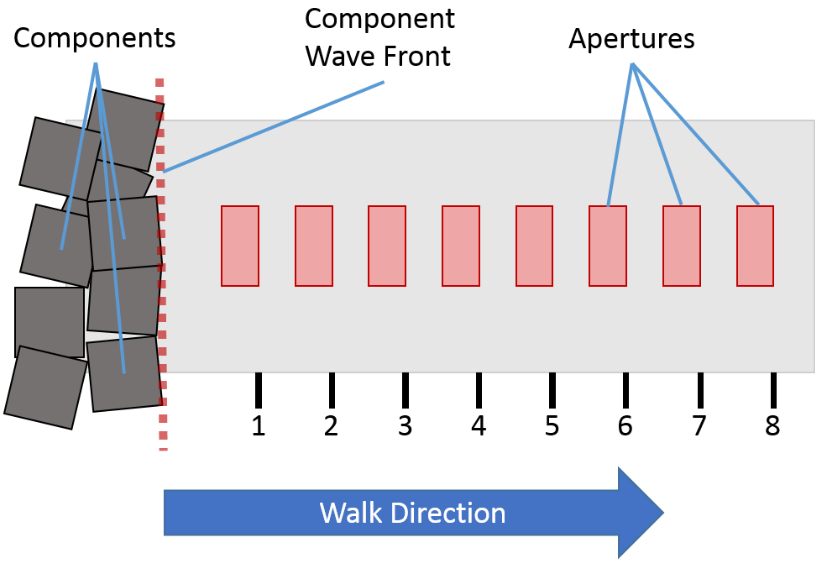

Figure 25. Single row of evenly spaced apertures.

In Figure 25, we have an assembly area with apertures evenly spaced into a row. If we were to perform walking mode in the direction prescribed, the total number of components successfully delivered will simply be:

$$T(x) = x \tag{9}$$

Where T is the total number of components delivered, and x is the position of the component wave front, in the arbitrary distance-unit used in Figure 25. We can apply a similar analysis on the open-loop walking mode experiment presented in 3.1.3. From the layout of the 200-trap assembly area used in 3.1.3 (Figure 26a), we mark the distance traveled along the diagonal, from the top-left corner to the lower-right corner of the assembly area, and account for the number of apertures at said distances, as shown in Figure 26b.

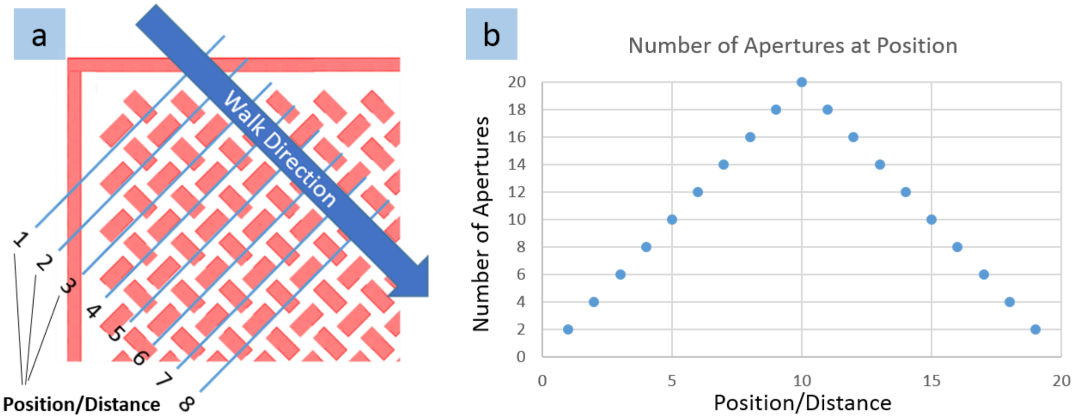

Figure 26. Analysis of the positions of apertures in 200-trap assembly area; ***a****: layout of 200-trap assembly area used in 3.1.3, superimposed with the walking direction and position/distance traveled, along said direction;* ***b****: the number of apertures located along each position along the direction of walking.*

We plot the number of delivered components as a function of the position of the component wave front, as it travels along the prescribed walking direction. The cumulative number of components delivered into empty apertures is plotted in Figure 27.

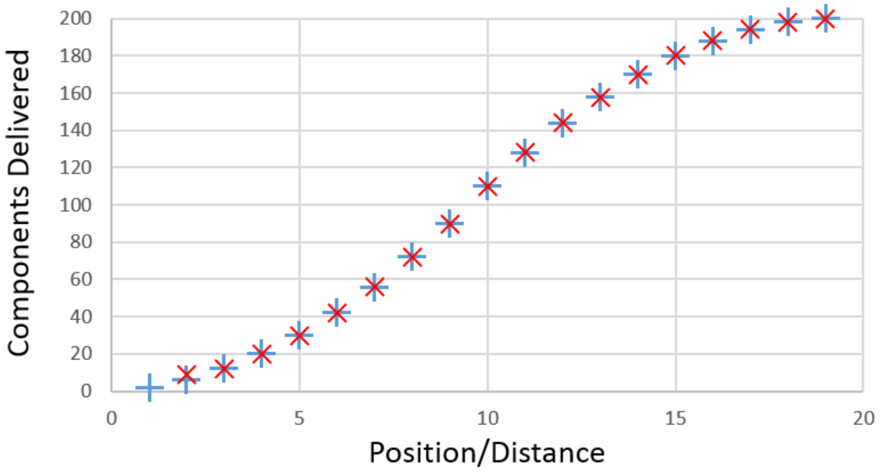

Figure 27. Components delivered into apertures, as a function of position/distance traveled along prescribed walking direction. ×s: (data) average fill of apertures behind the component wave front, averaged over 10 walking mode experiments; +s: (model) theoretical total number of apertures traversed, at each position/distance traveled along the prescribed walking direction (cumulative summation at various positions of Figure 26b). Note: we are unable to get × data for position 1; at the beginning of walking mode experiments, the top-left corner of the assembly area is often already filled due to the space confines of the assembly area.

In Figure 27, we compare the experimental data (×s, average fill of apertures behind position of component wave front) with the theoretical total number of apertures traversed (the model, +s), at each position/distance traveled along the prescribed walking direction. The experimental data agrees very well with our assertion that the total number of parts delivered is a function of the position of the component wave front, with the exception of positions 1 and 2, where apertures are often filled before the experiment due to the crowding of components in the vicinity.

For walking mode deliveries, we can analyze any arbitrary assembly region and figure out the total number of components delivered based on the position of the component wave front, relative to the initial position. Given that we can easily track the front of the wave of excess components with image processing, we can easily integrate this model into any automated control systems, for assembly regions of any arbitrary component placement.

3.2 Template-based Assembly of 01005 Components

The conditions at which micro-components can be manipulated with our modified linear actuator setup are determined by sweeping through actuation frequencies, and identifying the motion modes (and directions, in the case of walking and jumping modes) that occurs at specific frequencies. At each identified frequency, the amplitude of the input signal is then swept to tune for the desired velocities.

To demonstrate that our template-base self-assembly method is a complete “self-assembly” process, as defined earlier, which includes a transportation/delivery step, a self-alignment step, and a permanent adherence step, we adapted the component delivery system introduced above to the assembly of surface mount technology (SMT) thin-film resistors and monolithic ceramic capacitors of the 01005 standard (0.016" × 0.008", 0.4 mm × 0.2 mm).

The impetus for assembling SMT components directly onto chips is, firstly, an alternative for designers to not have to “off-chip” large capacitive and resistive elements in their circuits onto printed circuit boards (PCBs), thereby improving overall device performance. Secondly, SMT components also offer much better property tolerances than integrated passive elements which suffer heavily from process variations (typically at least 10%, on the same wafer [33]).

In this case, we employed two assembly templates, as shown in Figure 30, and apply similar design-rules for the traps as previously introduced.

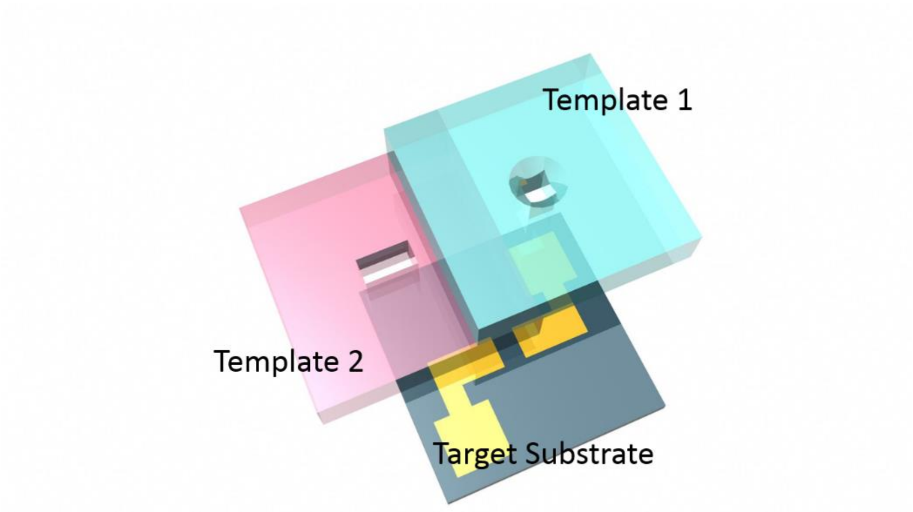

Figure 28. Dual Templates: Template 1 captures a component at a specific location over the Target Substrate. Template 2 guides the SMT component to fall in the correct direction.

3.2.1 Fabrication of Target Substrate for SMT Assembly

The fabrication process of Template 1 is similar to section 3.1.1, and the fabrication of Template is a straightforward DRIE through-etch. The fabrication of the Target Substrate (Figure 28) is as shown in Figure 29.

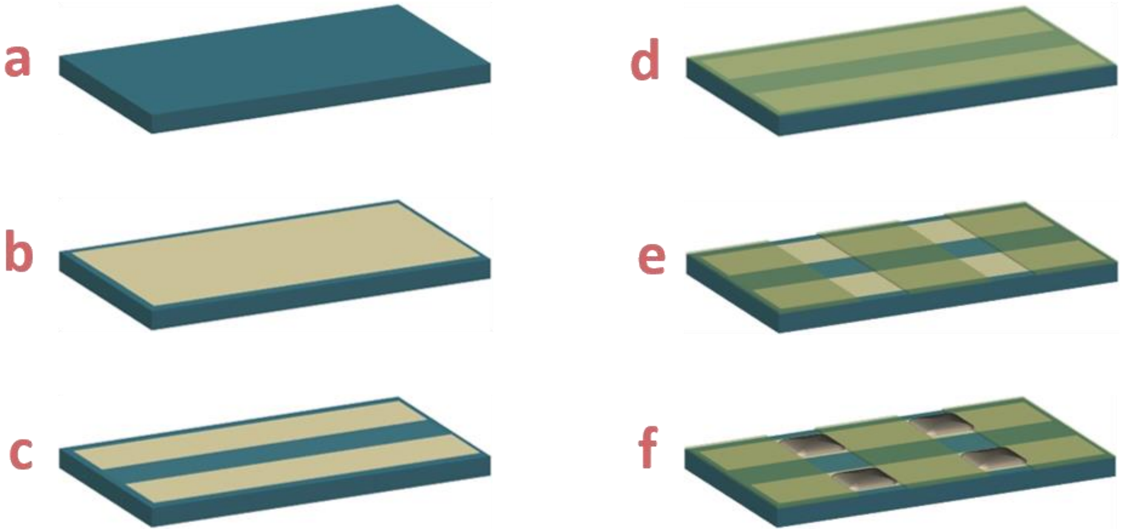

Figure 29. Fabrication process of Target Substrate (parallel-circuit) for SMT Assembly: ***a****. silicon wafer;* ***b****. silicon wafer is deposited with a layer of gold;* ***c****. gold layer is patterned;* ***d****. Su-8 is deposited;* ***e****. openings are made in the Su-8 layer for contact pads;* ***f****. 60 °C solder is dip-coated onto exposed gold surfaces.*

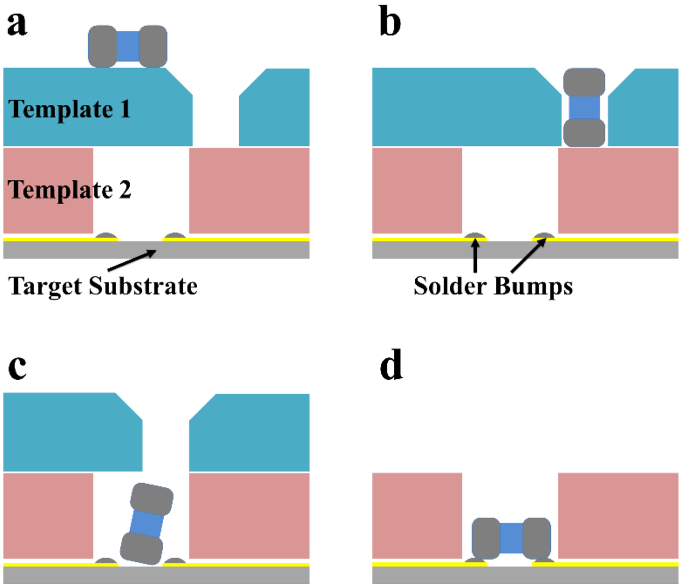

Figure 30. Assembly process: ***a****. walking mode component delivery performed on Template 1;* ***b****. a single component is captured by Template 1 near the binding location;* ***c****. by shifting Template 1, the component is allowed to drop into template 2;* ***d****. slightly agitating the system aligns the component to the orientation of the aperture on top of the binding location on the target substrate. After step* ***d****, solder reflow is performed to bond the component to the target substrate mechanically*

and electrically.

Template 1 captures a single component over an assembly location, while Template 2 guides the component to fall on its side with the correct orientation for permanent adherence. To match the dimensions of 01005 components, thereby preventing an additional component from getting partially trapped by each slot, Template 1 was fabricated with 400 µm thick silicon wafers. There is no such thickness requirement for Template 2.

After the components that are captured by Template 1 are transferred into Template 2 (Figure 30c), additional agitation is applied to the system to enable the SMT components to fall on their sides, resting their electrodes onto the solder bumps. During this step, Template 1 may be removed, thereby allowing the use of visual feedback to ensure that all SMT components have fallen on their sides, properly aligned for solder-reflow.

During the solder reflow process, the molten solder wets the metallized contact-ends of the SMT components and aligns them to the contact pads on the target substrate. 60 °C In-Bi-Sn solder was used in our experiments. At the end of the solder reflow, mechanical and electrical bonds between components and substrate were achieved, completing the transport, alignment and bonding stages of a self-assembly process.

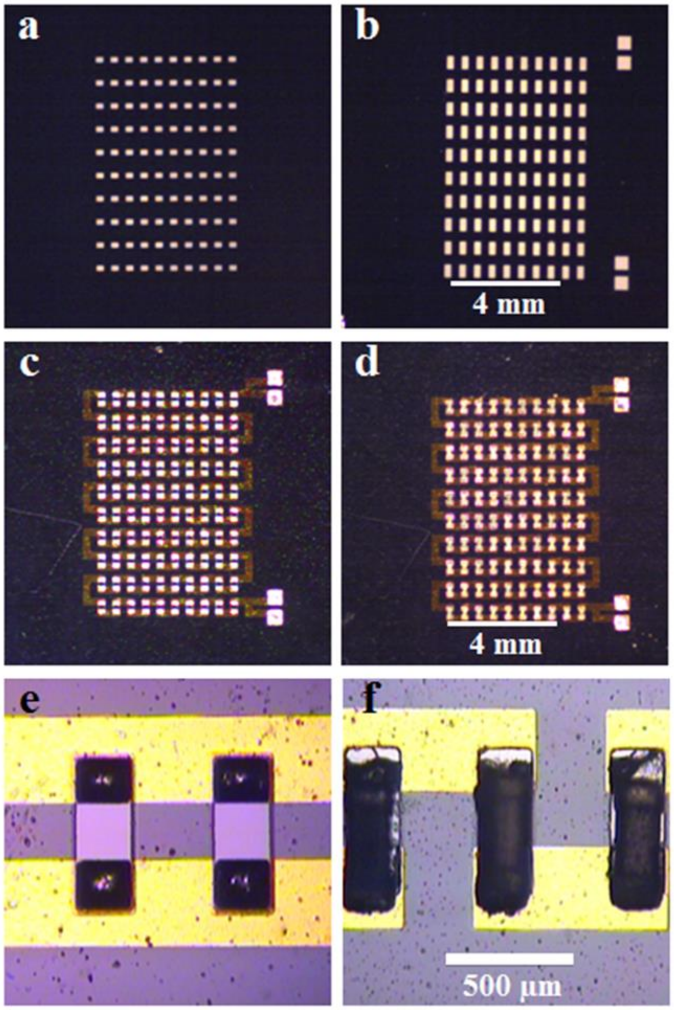

Figure 31. ***a****. Template 1 for a 100-component series-connection circuit;* ***b****. Template 2;* ***c****. empty target substrate;* ***d****. Target substrate with 100 01005 capacitors assembled;* ***e****. close-up view of parallel-connection circuit target substrate;* ***f****. close-up view of series-connection circuit, assembled with 01005 capacitors.*

Using our template-based assembly method, we can reliably assemble circuits with many components, like in Figure 31, in a massively parallel fashion, thereby addressing the bottle-neck of the inefficiency of contemporary pick-and-place robotics with very small components like 01005 passives. The 100 components required in Figure 31a-d can be successfully delivered within 20 s. For much larger arrays, components may be introduced onto the assembly template at multiple locations, thereby aiding the distribution of components during the delivery process.

As with the silicon chips in section 3.1.2, we can either use pre-programmed open-loop assembly sequences that virtually guarantee complete assembly, or employ visual feedback to redirect free components to fill unoccupied traps.

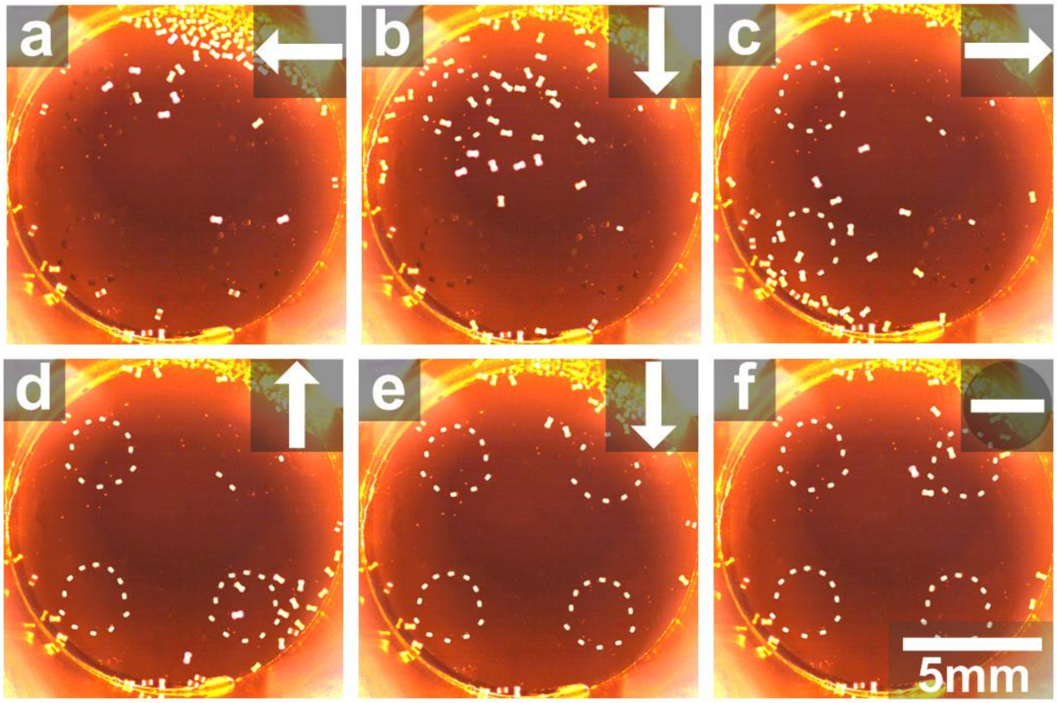

*Figure 32. Delivery of SMT components into the Template 1 apertures of circular test circuits with 48 components using feedback driven assembly (section 3.1.2); arrows in each frame indicate the direction in which the SMT components are driven: **a**. assembly begins with parts being driven to the left from the top right corner; **b**. after the components for the top left ring have been delivered, the parts are driven downwards to the bottom left; **c**. rightwards; **d**. upwards; **e**. now that most of the excess parts are located above the top right ring, we drive the parts downwards, as some sites in the top right ring remained vacant after step d; **f**. delivery completed. 100% excess parts has been used in this assembly (96 components used).*

Another challenge for contemporary pick-and-place robotics is the ability to perform component placement at arbitrary in-place orientations. Our methodology also supports arbitrary in-plane orientation for the assembly of SMTs, enabling greater flexibility with component placement/assembly, as shown in Figure 32 and Figure 33.

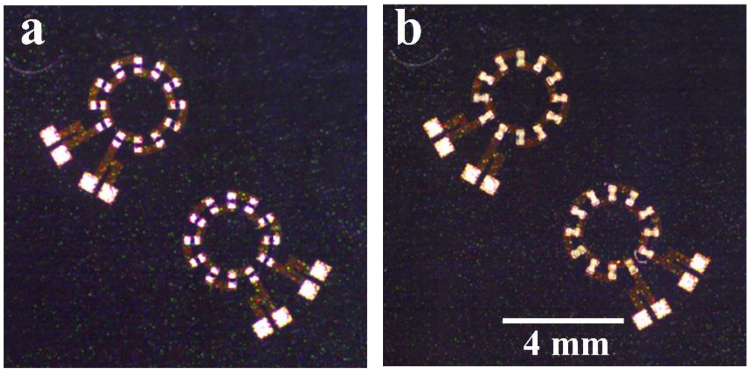

*Figure 33. **a**. Target substrate of circular 12-component series-connection circuit; **b**. 01005 capacitors assembled target substrate of circular 12-component series-connection circuit.*

To test the electrical fidelity of our self-assembled components, we built test circuits with 10 SMT components assembled in series and in parallel (Figure 34).

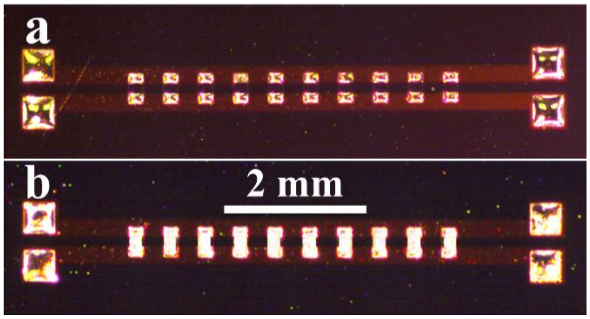

*Figure 34. A 10-component parallel test circuit before (**a**) and after (**b**) the assembly of 01005 100 kΩ resistors.*

In Figure 34 we probe the effective resistance across 10 100 kΩ resistors assembled in parallel; the resistance of the circuit is measured each time a resistor is pried from the circuit. Figure 12 shows the effective resistance of the test circuits against the number of resistors left intact (not pried off). The result in Figure 35 verifies that electrical connectivity is established with our assembly process.

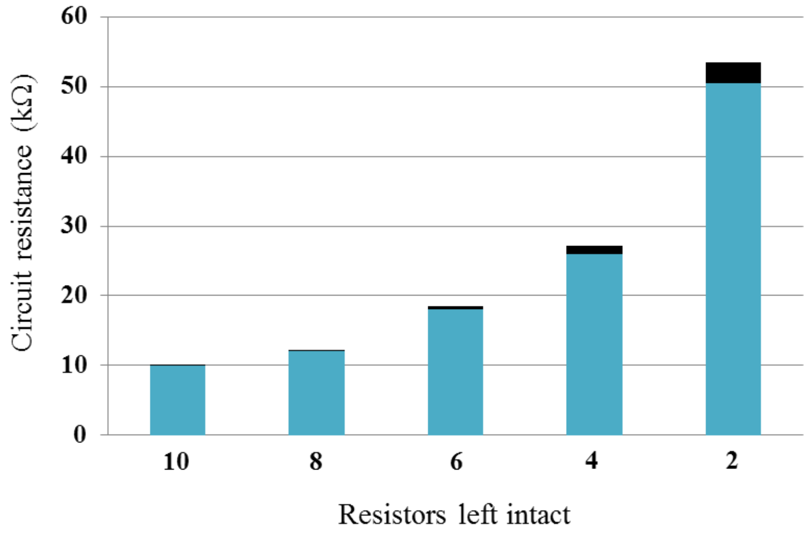

Figure 35. Average effective resistance of 10 100 kΩ resistors on 5 parallel test circuits (Figure 34b). Variances are indicated with the black segments on top of each bar.

The choice of a tertiary, low melting temperature solder (60 °C, In-Bi-Sn) is made for the flexibility it accords through the ability to place solder bumps on our test devices with conventional laboratory equipment (dip-coater), and thus reduced prototyping turnaround time. The mechanical strengths of our reflowed solder bonds were significantly weaker, and more inconsistent, than those found on surface mounted devices on the PCBs of commercial electronics. This is likely due to the presence of the many intermetallic boundaries and oxides associated with such tertiary solders. Mechanical tests on our solder-bond strength will be meaningful when stronger, higher temperature binary solders (typically Au-Sn) are used in our assembly process.

3.3 Conclusion

We present template-based microscale self-assembly as a viable technique that promotes the electronics industry's initiative towards functional diversification and function densification. We establish foundational work that enables programmable test-component delivery to receptor sites with a batch assembly process that leads to 100% yield within tens of seconds. The delivery mechanism is statistically characterized and a chemical kinetics inspired model is developed. Our template-based self-assembly method is then adapted to assemble standard 01005 format (0.016" × 0.008", 0.4 mm × 0.2 mm) monolithic ceramic capacitors and thin-film resistors onto silicon substrates. This process is CMOS compatible and is competitive with capacitors and resistors fabricated through standard foundry processes.

CHAPTER 4. HIGH DENSITY INTEGRATION OF SURFACE MOUNT TECHNOLOGY COMPONENTS IN THROUGH-SILICON TRENCHES

4.1 Introduction

In section 3.2, we reported the template-based parallel assembly of SMT (surface mount technology) components onto die surfaces [22], providing a solution for the assembly of capacitors and resistors directly onto chips (Figure 36a), instead of having designers to "off-chip" large capacitive and resistive elements in their circuits onto printed circuit boards (PCBs), thereby improving overall device performance. SMT components also offer much better property tolerances than integrated passive elements that suffer heavily from process variations (typically at least 10%, on the same wafer [33]).

Based on a study of the assembly of nickel TSVs (through-silicon vias) using magnetic force presented by Fischer et al. [29], we extend on our chip-surface assembly to include the assembly of 01005 passive components into vertical trenches etched through the die. By assembling SMT components in deep trenches, our methodology accesses chip-volume that would otherwise not be utilized. Using well-established passive components, we avoid having to perform material development and integration (exotic high-κ dielectric materials, for example) into existing foundry processes. Furthermore, the through-die trenches we require are very similar to those used in TSVs, allowing our process to be easily adopted by foundries already offering TSV solutions.

4.2 Assembly Process Flow

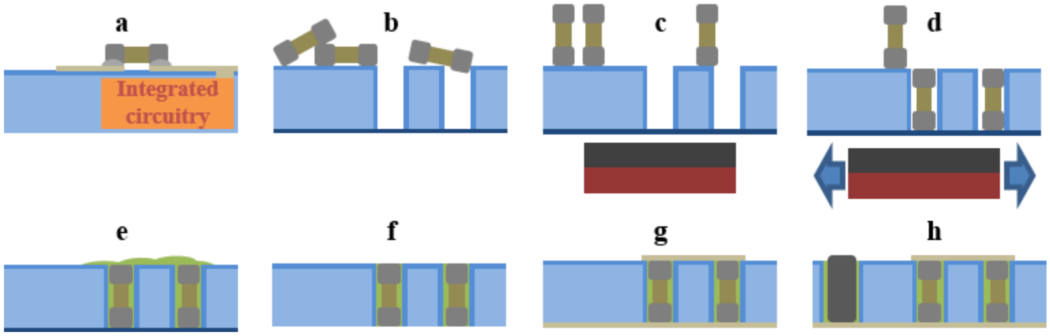

Figure 36. ***a****. On-die/chip SMT assembly methodology previously introduced [22].* ***b*** *–* ***h****: Through-silicon trench SMT assembly process flow;* ***b****. SMT components are distributed on through-etched wafer set on wafer-processing tape;* ***c****. magnet is introduced on back-side of twafer;* ***d****. magnetic force from magnet drags components across wafer surface, and into trenches;* ***e****. fill-material is applied and cured;* ***f****. excess material on the surface as well as wafer-processing tape is removed;* ***g****. metallization is performed on the front and back sides of wafer;* ***h****. TSVs can be similarly assembled to access the metal layer on the back-side.*

01005 components are first distributed onto a wafer which is set on wafer processing tape, prepared with corresponding vertical trenches etched through its thickness (Figure 36b). Magnetic force is introduced to pull the components into the trenches (Figure 36d, Figure 37). Fill material, like BCB (benzocyclobutene) based thermosets, is applied and cured to permanently confine the “entrenched” components. Excess fill material is then removed from the front face of the wafer with plasma etching and the wafer processing tape is also removed from the back face. Metallization is performed on the front and back faces to form the desired circuitry (Figure 36g). TSVs may be employed to access the metal layer on the back of the die (Figure 36h); in particular, if Nickel TSVs are permissible, the methodology presented by Fischer et al. [29] will be compatible with our assembly process.

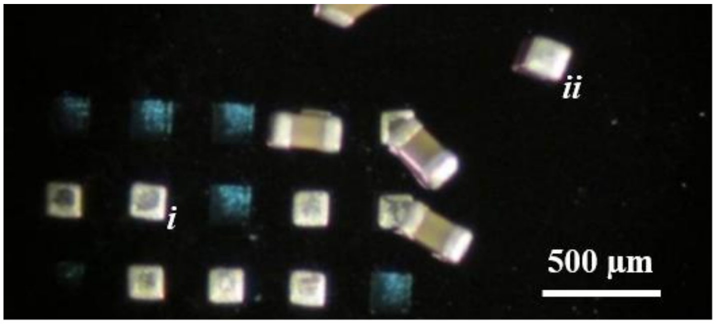

Figure 37. Trench array filling in progress; 01005 capacitors are manipulated with magnetic forces. ***i*** *marks an example of a component trapped within a vertical trench.* ***ii*** *shows a component standing upright on the surface of the silicon chip.*

Figure 37 shows SMT capacitors being manipulated by the presence of a magnet underneath the chip. In our experiments, we attach a NeFeB, Grade N48 rare earth magnet on top of an orbital shaker. Test chips (with SMT components distributed randomly on the surface) are held at 2 mm above the magnet while the orbital shaker is activated, thus moving the components on the chip surface with magnetic force in a circular motion. The maximum magnetic field experienced by a component is derived through simulation to be about 0.7 T, and the corresponding force applied on a component is calculated to be about 16 µN. The assembly setup is shown in Figure 38.

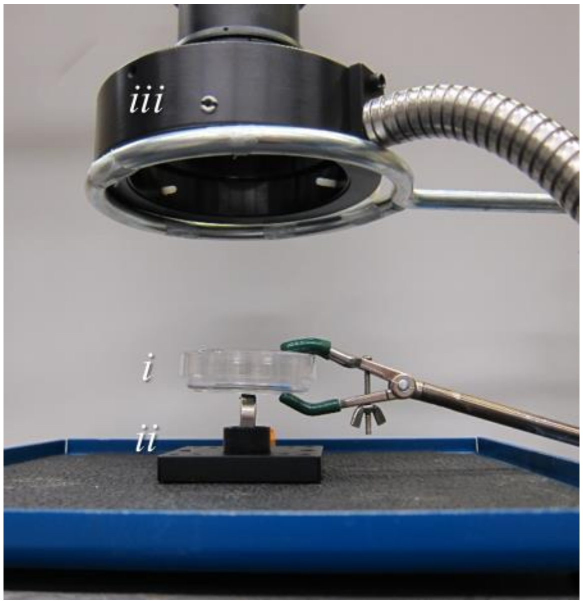

Figure 38. Magnetic assembly setup: ***i****. translucent container holding test chip and SMT components;* ***ii****. NeFeB Grade N48 rare-earth magnet attached to orbital shaker;* ***iii****. lighting and visual equipment.*

By design, the depth of the trenches is very close to the length of the SMT components, thus preventing captured components from obstructing the movement of free components.

Excess spaces in the occupied trenches are filled by a manual application of BCB CYCLOTENE® 3022-46. The resin was degassed in a vacuum chamber and cured in a vacuum oven to prevent the formation of voids in the cured polymer.

Plasma etching was performed to remove excess resin and expose the SMT contacts. Having precisely matched the thickness of our test chips to the length of the SMT components, we avoided having to perform grinding and polishing as reported in [29] (Fischer et al. had nickel wires that were significantly protruding from the surface of their wafer) to planarize our chips for subsequent metallization.

Aluminum was evaporated onto the front and back sides of the chips to establish electrical connections.

Classifying this self-assembly work per section 1.2 gives us a delivery mechanism driven largely with magnetic forces, while component alignment, before permanent adherence, is achieved during the introduction and curing of fill-materials. Such a combination of delivery and alignment mechanisms is unique, compared to the works surveyed in 1.3.

4.3 Experimental Design

To investigate the influence of the design of trench arrays on the delivery of components to said trenches, we fabricated four array designs with different trench sizes and trench-to-trench spacing distances as listed in Table 5.

Table 5. Specifications of our experimental designs; the capacitance per area C for each design is calculated by dividing capacitance per component (10 nF) by its area footprint ((T + S)^2, based on Figure 39).

Design	**Trench Size *T* (μm)**	**Trench Spacing *S* (μm)**	***C*** **(pF·μm^{-2})**
A	**230**	**150**	**69**
B	**230**	**250**	**43**
C	**300**	**150**	**49**
D	**300**	**250**	**33**

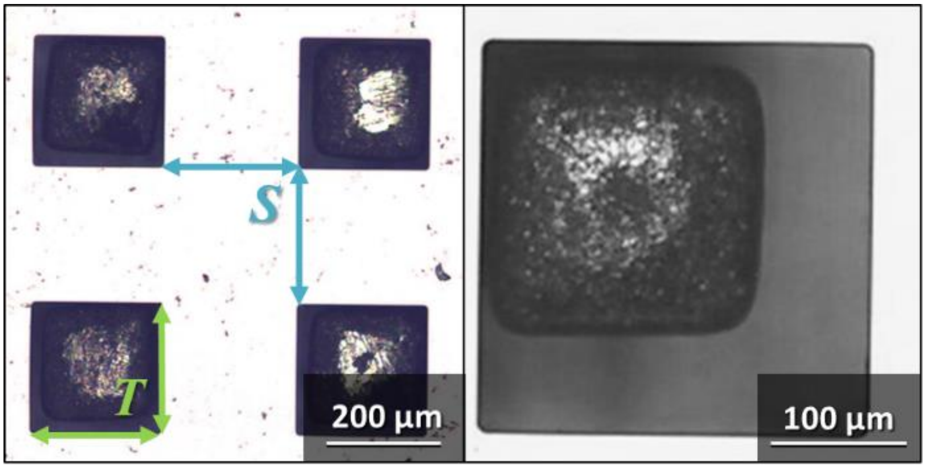

Figure 39. 01005 capacitors in 230 × 230 trenches (Design B) on the left, and 300 × 300 trench (Designs C, D) on the right. T indicates trench size, and S indicates trench spacing.

We calculate the capacitance per unit area for each of our four designs in order to compare the effective capacitance of our assembled arrays (using off-the-shelf 10 nF 01005 capacitors) with a theoretical benchmark for integrated capacitors [30].

4.4 Theoretical Benchmark for Integrated Capacitors

To benchmark the performance of our assembled capacitor arrays, we employ the models introduced by Aparicio and Hajimiri [30] on the theoretical upper-bounds for the maximum capacitance that can be derive from rectangular (Manhattan) capacitor structures fabricated using regular planar processes. Calculations based on a typical 130 nm foundry CMOS process are tabulated in Table 6.

Comparing Table 5 and Table 6, our assembled capacitors clearly out-perform the theoretical maximum capacitance of oxide and nitride capacitors, even when considering an improbable integrated capacitor made with 9 layers of metal. The comparison is even more favorable when our calculated values are placed against the “semi-empirical model” which is more realistic as it takes into account the physical limitations of integrated capacitors [30].

*Table 6. Maximum possible capacitance per micrometer-squared of typical 130 nm foundry CMOS process [30] (parameters: minimum width of features = 0.18 µm; thickness of each layer of metal/dielectric = 0.35 µm). * indicates “semi-empirical” variant of the model that takes into account the physical limitations of parallel-plate capacitors.*

Layers of Metal	**Oxide (ε_r = 3.9)**		**Nitride (ε_r = 7.5)**	
	C_{max} (pF·µm^{-2})	**C_{max}* (pF·µm^{-2})**	**C_{max} (pF·µm^{-2})**	**C_{max}* (pF·µm^{-2})**
2	**1.14**	**0.72**	**2.44**	**1.55**
3	**1.90**	**1.20**	**4.06**	**2.58**
5	**3.41**	**2.17**	**7.31**	**4.64**
9	**6.44**	**4.09**	**13.81**	**8.77**

4.5 Results and Discussion

4.5.1 Component Delivery

The results of experiments of the delivery of SMT components into 21 by 21 arrays of trenches of designs A, B, C and D are shown in Figure 40.

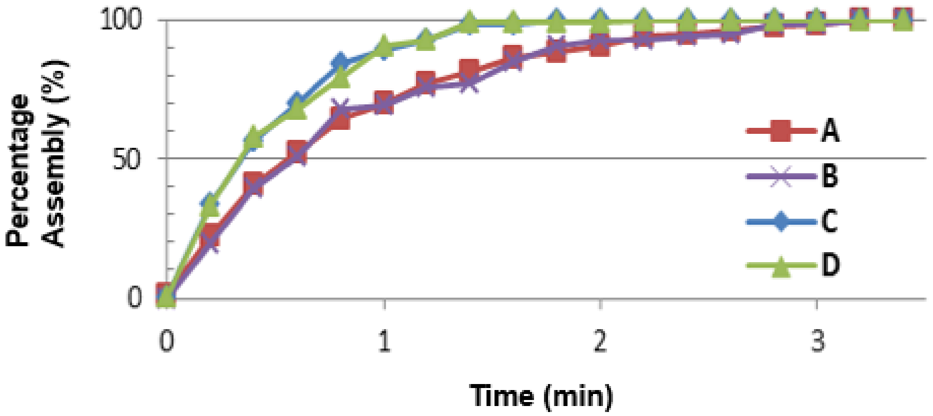

Figure 40. Percentage assembly of components (20% excess parts) into 21 × 21 arrays of various designs (Table 5) over time (averaged over 5 runs per design).

Figure 40 shows the percentage completion of the array designs over time. Experimentally extracted first order rate constants for curves A, B, C and D are 0.65 s^{-1}, 0.46 s^{-1}, 0.80 s^{-1}, and 0.81 s^{-1} respectively (CHAPTER 3). It is observed that, out of the two design parameters, trench separation has no significant influence over the speed with which the arrays are being filled. Thus, it is possible to create grids with tighter trench separation for even greater component density and achieve greater capacitance/resistance per unit area without sacrificing the rate that the component arrays are assembled.

Partially and completely filled arrays are shown in Figure 41 and Figure 42.

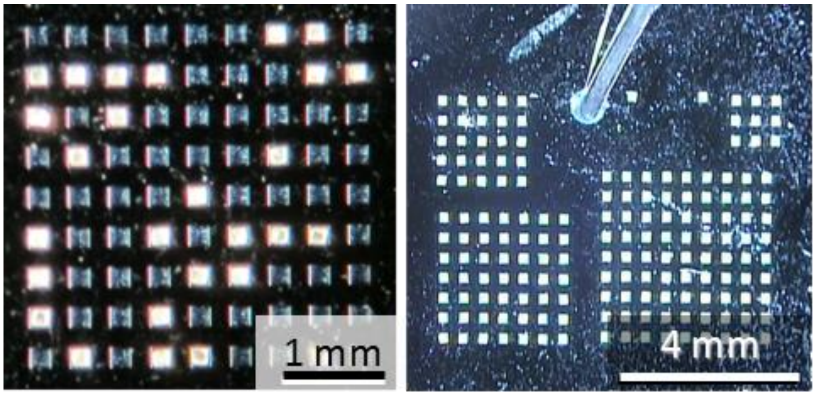

Figure 41. Left: Partially filled 9 × 9 A type array; Right: Completely filled 3 × 3, 5 × 5, 7 × 7, and 9 × 9 B type arrays.

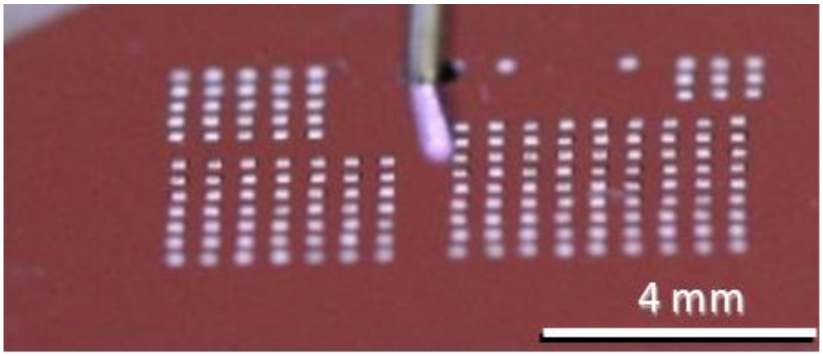

Figure 42. Perspective view of assembled 3 × 3, 5 × 5, 7 × 7, and 9 × 9 B type arrays.

4.5.2 Electrical Connectivity

To probe the electrical characteristics of our assembled capacitor arrays, a wire is attached to the metallized back-side of the test chips (Figure 43iii) through a specially prepared through-hole. Silver paste and solder were used to ensure ideal connectivity. The results are tabulated in Table 7.

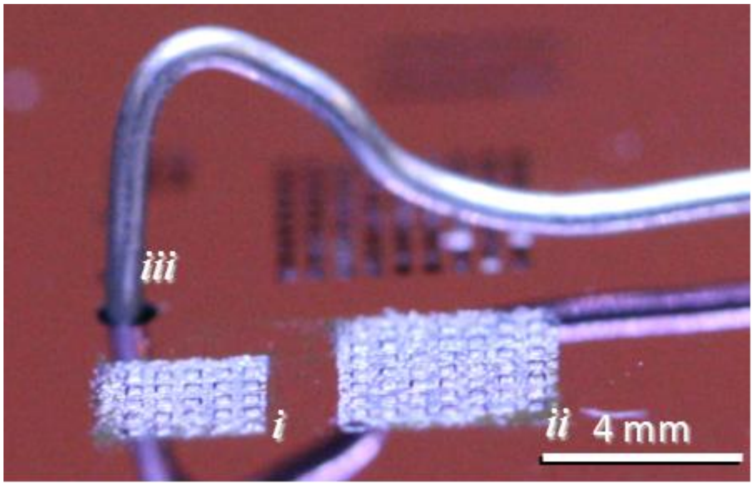

*Figure 43. Completed devices of 7 × 7 (**i**) and 9 × 9 (**ii**) B type arrays metallized with a final layer of aluminum. Wire (**iii**) is connected through the chip, to the back-side metallization of the chip for electrical testing.*

Table 7. Capacitance readings from SMT capacitor arrays, at: VDC = 0 V, VAC = 1 V, frequency = 100 Hz

Array Size	**Total Cap. (nF)**	**Std. Dev. (nF)**	**Average Cap. per component (nF)**
1	**10.14**	**0.17**	**10.14**
3	**30.82**	**0.33**	**10.27**
9	**93.48**	**0.91**	**10.39**
25	**261.68**	**5.83**	**10.57**

Capacitance readings from our SMT capacitor arrays were obtained using a HP 4263A LCR Meter at V_{AC} = 1 V driven at 100 Hz with a DC offset of 0 V. The average capacitance per component calculated from our arrays agrees with the stated capacitance of our 10 nF 01005 capacitors, verifying that our capacitor arrays are electrically viable.

4.5.3 Comparison with Existing Processes

Based on the theoretical upper bounds calculated for integrated capacitors in Table 6, it is obvious that, without significantly modifying a standard CMOS foundry process and introducing exotic high-κ dielectric materials, capacitance is very costly in terms of die area, justifying the need of circuit designers to place large capacitive requirements off-chip and onto PCBs. We believe that our on-die and in-die methodologies for the assembly of SMT passive devices can contribute to re-introduce the possibility of placing large capacitors and resistors in greater proximity of the integrated circuitry that requires them, thereby improving circuit response.

The advent of TSVs for die-stacking assembly and packaging solutions has introduced a growing number of CMOS foundries to through-etching wafers for TSVs; our proposed methodology is compatible with any TSV-able CMOS foundries.

We presented the superiority of using SMT capacitors in Table 5 and Table 6; our methodology can also allow circuit designers to place mega-Ohm resistors on die. Furthermore, SMT resistors are available at very tight tolerances (±1 %), and can help to partially alleviate current trends of up to 30 % deviation on product performance (due to process variations) even on mature platforms such as the 130 nm CMOS [34].

4.5.4 Future Work

To guarantee that every single trench is filled, we can adapt the software and hardware infrastructure developed in CHAPTER 3, and implement an automated feedback driven system. The system currently identifies unoccupied trenches and can direct free components towards them, ensuring 100% assembly. Our setup (Figure 38) will have to be modified, attaching the magnet to a 2 degrees-of-freedom device that can be controlled by the visual feedback system to drag SMT components to specified locations on the chip.

4.6 Conclusion

We report a method to deliver and assemble standard 01005 passives vertically into through-silicon trenches using batch assembly. Capacitors larger than is feasible with CMOS processes have been assembled, electrically tested, and compared against theoretical models. Capacitors with capacitances beyond what is feasible with CMOS processes have been assembled, electrically tested, and compared against theoretical models, enabling the placement of large capacitive requirements on-chip. Assembled capacitors also have better property tolerances than is possible with conventional CMOS. The assembly process may also be modified to implement a feedback-driven component delivery system previously introduced to ensure 100% assembly.

CHAPTER 5. CONCLUSION AND FUTURE WORK

5.1 Conclusion

The goal of this thesis work is to improve upon the mechanical agitation transport type self-assembly processes which our laboratory has previously investigated [27]. In our study, we refined the definition of microscale self-assembly to have the three distinct phases of the transportation, alignment, and permanent adherence of components, and assert that, for any processes that are at all useful for engineering purposes (of significant yields), there must be a sub-step within the transportation phase, which accepts correct and/or correctly oriented parts, and rejects incorrect/incorrectly oriented and excess components.

The initial approach was the introduction of catalytic components to the transportation phase of the assembly process (CHAPTER 2). Catalytic components have been demonstrated to enable stochastic micropart assemblies to be performed at energy levels lower than in cases without them, and thus allow assembly operations to be performed further from energy levels required for the disassembly of parts captured by receptors – ultimately improving assembly completeness. We also present an analytical framework inspired from chemical kinetics that can sufficiently explain the experimental data obtained.

We developed a programmable mechanical agitation transportation system which accords unprecedented control over the motion of microcomponents and can deliver them to receptor sites that leads to 100% yield within tens of seconds (CHAPTER 3). Based on data processed from experiments performed with silicon test parts (370 × 370 × 150 μm^3) the delivery mechanism is statistically characterized and a chemical kinetics inspired model is developed (section 3.1.3). The transportation of microcomponents to receptors can be guided with feedback, or performed with pre-programmed sequences in an open-loop setting.

The software and hardware infrastructure developed for the study of the silicon test parts above are then adapted for the assembly of standard 01005 format (0.016" × 0.008", 0.4 mm × 0.2 mm) monolithic ceramic capacitors and thin-film resistors onto silicon substrates (section 3.2). All three phases of self-assembly (as defined in section 1.2), transportation, alignment, and permanent-adherence, were performed in assembly of these SMT components, and electrical viability has been verified.

Finally, we present the assembly of SMT components into through-wafer trenches with a vertical pose (CHAPTER 4). By assembling SMT components in deep trenches, our methodology accesses chip-volume that will otherwise not be utilized. We then benchmarked assembled (composite) capacitors against the theoretical limit of integrated capacitors, and demonstrated that our assembled capacitors are competitive with capacitors fabricated with standard CMOS processes (section 4.5). Although the transportation phase is driven by magnetic forces (instead of linear vertical actuators in previous cases), established software and hardware infrastructure was easily adapted for analysis, and can be extended to provide feedback-driven control over component transportation.

5.2 Future Work

5.2.1 Full Automation for Closed Loop Component Delivery

While it is straightforward to program a set sequence of motions (jump/walk) towards various directions to implement an open loop component delivery process (e.g. Figure 21), closed loop delivery processes (e.g. Figure 20) currently require a human operator to observe the experiment and guide the assembly process (through a LabVIEW program).

While an extensive suite of MatLab® routines has been developed to process videos of experiments and account for every instance of the recorded assembly process, we do not yet have a real-time automated delivery guidance tool that can perform automated feedback driven component delivery due to current hardware limitations.

With an update of the high-speed camera setup, full automation for closed loop component delivery can be straightforwardly implemented, given that our current video/image processing software can already reliably account for all the information required (locations and number of empty/filled apertures, and locations and tally of free parts) to implement an automated closed loop delivery process.

5.2.2 Solid Model Simulation

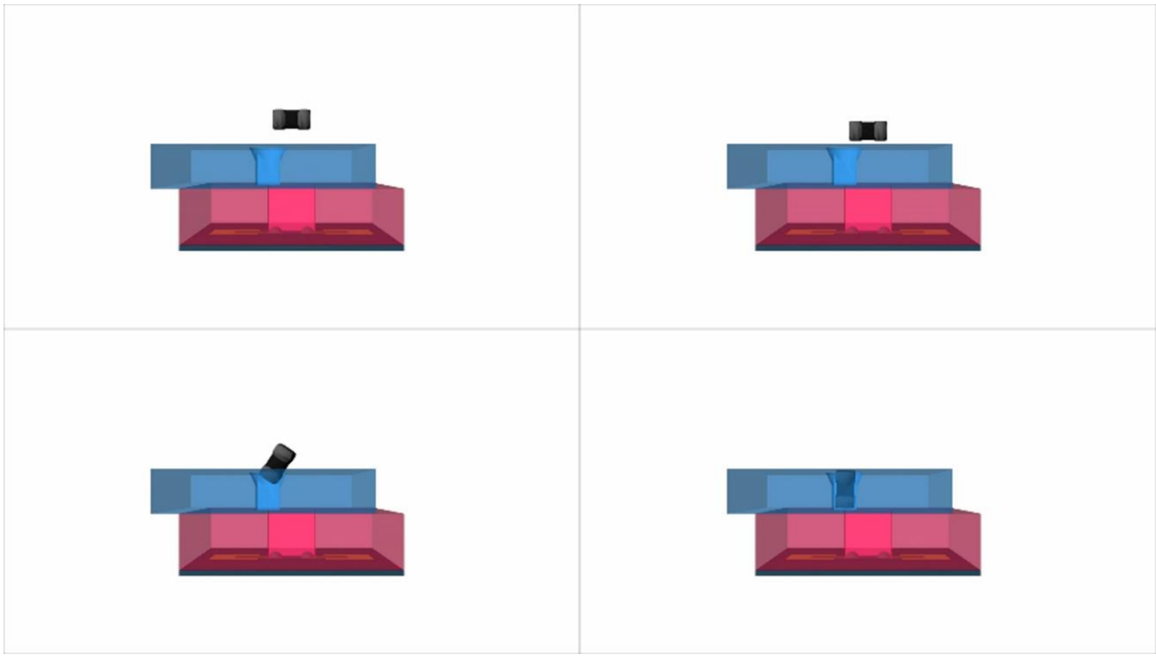

Figure 44. Animation sequence of 01005 SMT component falling into Template 1.

Throughout the dissertation work, we have used Maya® extensively to render layouts into 3D models. The Maya® 3D engine adequately handles the dynamics of interacting solid models, and allows us to create physically-reasonable simulations/animation sequences, as shown in Figure 44, which have been very helpful to illustrate our assembly processes.

However, if the effects of capillary and stiction forces can also be accurately implemented in these simulations, such solid model tools can be very helpful to the development of all, if not most, mechanical agitation transport type self-assembly processes; proposed process and components can be, at least partially, iterated through the use of simulations, thereby reducing time and resource expenditures on microfabrication.

5.2.3 Combining Self-assembly and Quantum-dots

In a separate project, we will be looking into the possibility of using silicon quantum-dot phosphors [35, 36] in electroluminescent (EL) lamps. It is plausible to use the transfer substrate previously mentioned (Figure 12) or the templates in [17, 18], to stochastically arrange silicon chips coated with silicon quantum-dots, and then transfer and embed them into a translucent polymer film as shown in Figure 45.

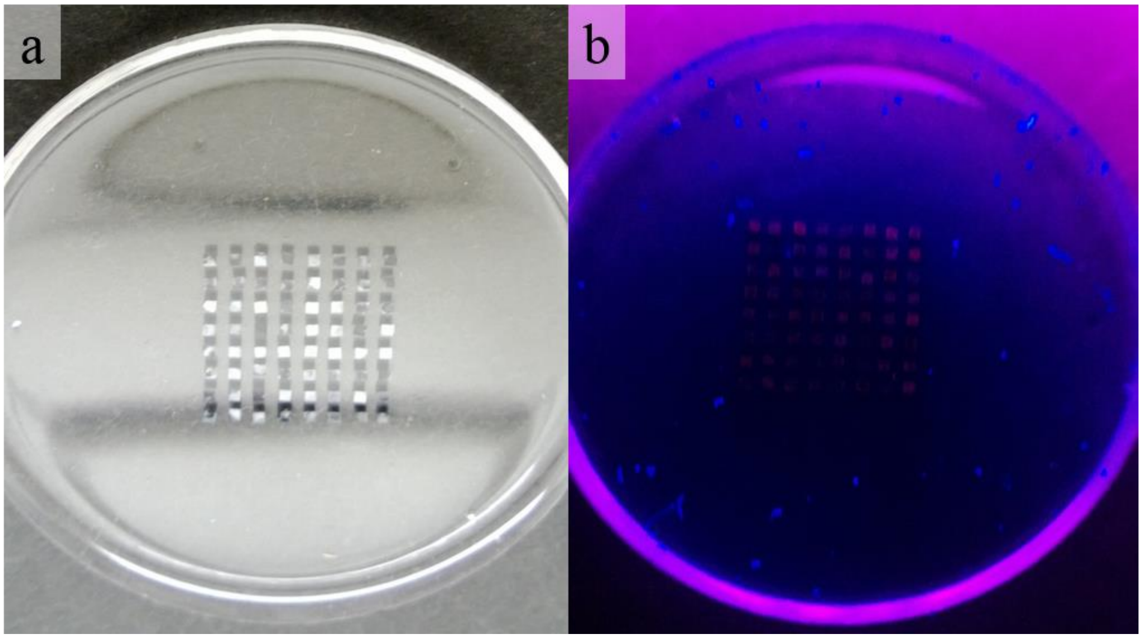

Figure 45. Silicon test-parts embedded in PDMS film: ***a****. normal illumination;* ***b****. ultraviolet illumination – reddish fluorescence due to presence of silicon quantum-dots on surface of the test-parts.*

While we have demonstrated photoluminescence in Figure 45, to implement electroluminescence, transparent conducting films will have to be employed, instead of the PDMS we use for a proof-of-concept demonstration.

5.3 A Vision for Self-assembly

5.3.1 Self-assembly as a Mainstream Process for Assembly and Packaging

With each publication about self-assembly, including this thesis, we hope to formalize the study of microscale self-assembly, such that it may soon become a mainstream process in the field of Packaging and Assembly for microelectronic devices.

For that to happen, potential users must have access to better computational tools (to be developed by researchers in self-assembly) which can quickly analyze the feasibility of self-assembly, given a set of components to assemble on a particular substrate; in other words, to quickly derive a cost-comparison for stochastic microscale self-assembly versus the conventional method, which is mostly pick-and-place. Towards that goal, in this thesis and several forthcoming publications, we introduce the framework of breaking-down and analyzing self-assembly processes as distinct stages, and add to the growing library of studies in the theory of self-assembly; our study on the effect of catalysis in microscale self-assembly may also count towards the advancements in the theoretical basis of the field.

A significant milestone for the community/field would be when “self-assembly” enters the mainstream lexicon for the microelectronics industry, and beyond, such that when new patents based on stochastic microscale self-assembly processes are filed, they will be duly referred to as such.

5.3.2 Synergies with 3D Printing Technologies

More broadly, beyond building on themes mentioned in the thesis, we predict synergies between self-assembly and the emergent technology of 3D printing [37]. Technology in the realm of 3D printing is advancing very rapidly, and is quickly becoming competitive with traditional manufacturing in terms of cost [38], precision [39], and applications [40]. 3D printing technologies will enable new possibilities in the types of substrates and devices that are available and applicable for self-assembly processes.

Analogous to the fact that not all device-types can be integrated on a single type of substrate, we can assert that not all material-types can be processed into a format that is applicable for 3D printing, thus ensuring that 3D printing will be complementary, and not substitutive, to assembly and self-assembly.

REFERENCES

1. Morris, C.J., Stauth, S.A., and Parviz, B.A., *Self-assembly for microscale and nanoscale packaging: steps toward self-packaging.* IEEE Transactions on Advanced Packaging, 2005. 28: p. 600 - 611.
2. Fearing, R.S., *Survey of sticking effects for micro parts handling*, in *Proceedings of the International Conference on Intelligent Robots and Systems-Volume 2 - Volume 2*. 1995, IEEE Computer Society. p. 2212.
3. Zhirnov, V.V., et al., *Limits to binary logic switch scaling - a gedanken model.* Proceedings of the IEEE, 2003. 91(11): p. 1934-1939.
4. Arden, W., et al. *"More-than-Moore" White Paper*. 2010,[cited; Available from: http://www.itrs.net/papers.html.
5. Kenneth W Economy, R.A.N., Richard L Bumann, (Unisys Corporation), Vibrating Template Method of Placing Solder Balls on the I/O Pads of an Integrated Circuit Package, 5839191, 1997.
6. David J. Klossner, M.J.Y. (International Business Machines), Direct Vertical Pin Feeder, 5176289, 1993.
7. Fukushima, T., et al. *Multichip self-assembly technique on flexible polymeric substrate*. in *Electronic Components and Technology Conference, 2008. ECTC 2008. 58th*. 2008.
8. Whitesides, G.M. and Grzybowski, B., *Self-Assembly at All Scales.* Science, 2002. 295(5564): p. 2418-2421.
9. Hoo, J.H., et al. *Programmable self-assembly for microsystem integration*. in *Solid-State Sensors, Actuators and Microsystems Conference (TRANSDUCERS), 2011 16th International*. 2011.
10. Knuesel, R.J. and Jacobs, H.O., *Self-assembly of microscopic chiplets at a liquid-liquid-solid interface forming a flexible segmented monocrystalline solar cell.* Proceedings of the National Academy of Sciences of the United States of America, 2010. 107(3): p. 993-998.
11. Saeedi, E., Kim, S., and Parviz, B.A., *Self-assembled Crystalline Semiconductor Optoelectronics on Glass and Plastic.* Journal of Micromechanics and Microengineering, 2008. 18: p. 7.
12. Xiong, X., et al., *Controlled multibatch self-assembly of microdevices.* Journal of Microelectromechanical Systems, 2003. 12(2): p. 117-127.
13. Saeedi, E., Etzkorn, J.R., and Parviz, B.A., *Sequential self-assembly of micron-*

scale components with light. Journal of Materials Research, 2011: p. 268 - 276.

14. Yeh, H.J.J. and Smith, J.S., *Fluidic self-assembly for the integration of GaAs light-emitting diodes on Si substrates.* Photonics Technology Letters, IEEE, 1994. 6(6): p. 706-708.
15. Srinivasan, U., Liepmann, D., and Howe, R.T., *Microstructure to Substrate Self-Assembly Using Capillary Forces.* JOURNAL OF MICROELECTROMECHANICAL SYSTEMS, 2001. 10: p. 17-24.
16. Jacobs, H.O., et al., *Fabrication of a Cylindrical Display by Patterned Assembly.* Science, 2002. 296(5566): p. 323-325.
17. Kwang Soon, P., et al., *Mechanics and Scaling of thin part Assembly at a Fluidic Interface.* Journal of Micromechanics and Microengineering, 2011. 21(2): p. 025002 (7 pp.).
18. Kwang Soon, P., et al., *Parallel heterogeneous integration of chip-scale parts by self-assembly.* Journal of Microelectromechanical Systems, 2012. 21(6): p. 1273-5.
19. Kwang Soon, P., et al., *Orientation-controlled parallel assembly at the air-water interface.* Journal of Micromechanics and Microengineering, 2012. 22(10): p. 105028 (11 pp.).
20. Kwang Soon, P., et al., *Optimization of Angular Alignment in Self-Assembly of Thin Parts at an Air-Water Interface.* Journal of Microelectromechanical Systems, 2013. 22(1): p. 13-15.
21. Hoo, J., Baskaran, R., and Böhringer, K.F. *Programmable Batch Assembly of Microparts with 100% Yield*. in *Transducers*. 2009. Denver, CO.
22. Hoo, J., et al. *Parallel assembly of 01005 surface mount technology components with 100% yield*. in *IEEE International Conference on Micro Electro Mechanical Systems (MEMS)*. 2010.
23. Ramadan, Q., Uk, Y.S., and Vaidyanathan, K., *Large scale microcomponents assembly using an external magnetic array.* Applied Physics Letters, 2007. 90(17): p. 172502/1-172502/3.
24. Morris, C.J. and Parviz, B.A. *Micro-scale system integration via molten-alloy driven self-assembly and scaling of metal interconnects*. 2007. Piscataway, NJ 08855-1331, United States: Institute of Electrical and Electronics Engineers Computer Society.
25. Kwang Soon, P., et al., *Effect of Fluid Viscosity on Dynamics of Self-Assembly at Air-Water-Solid Interface.* Journal of Microelectromechanical Systems, 2013.

22(3): p. 662-9.

26. Fang, J. and Böhringer, K.F., *Wafer-level packaging based on uniquely orienting self-assembly (the DUO-SPASS processes).* Microelectromechanical Systems, Journal of, 2006. 15(3): p. 531-540.
27. Fang, J. and Böhringer, K.F., *Parallel micro component-to-substrate assembly with controlled poses and high surface coverage.* Journal of Micromechanics and Microengineering, 2006. 16(4): p. 721-730.
28. Wang, K., Baskaran, R., and Böhringer, K.F. *Template Based High Packing Density Assembly for Microchip Solid State Cooling Application*. in *3rd Annual Conference on Foundations of Nanoscience: Selfassembled Architectures and Devices (FNANO)*. 2006. Snowbird.
29. Fischer, A.C., et al., *Very high aspect ratio through-silicon vias (TSVs) fabricated using automated magnetic assembly of nickel wires.* Journal of Micromechanics and Microengineering, 2012. 22(10): p. 105001 (9 pp.).
30. Aparicio, R. and Hajimiri, A., *Capacity limits and matching properties of integrated capacitors.* Solid-State Circuits, IEEE Journal of, 2002. 37(3): p. 384-393.
31. Baskaran, R., et al. *Catalyst enhanced micro scale batch assembly*. in *IEEE International Conference on Micro Electro Mechanical Systems (MEMS)*. 2008.
32. Steinfeld, J.I., Francisco, J.S., and Hase, W.L., *Chemical Kinetics and Dynamics*. 2 ed. 1998, Upper Saddle River, New Jersey: Prentice-Hall, Inc. 518.
33. Cheng, Y. *The influence and modeling of process variation and device mismatch for analog/rf circuit design*. in *Devices, Circuits and Systems, 2002. Proceedings of the Fourth IEEE International Caracas Conference on*. 2002.
34. Datta, A., et al. *Speed binning aware design methodology to improve profit under parameter variations*. in *Design Automation, 2006. Asia and South Pacific Conference on*. 2006.
35. Resch-Genger, U., et al., *Quantum dots versus organic dyes as fluorescent labels.* Nat Meth, 2008. 5(9): p. 763-775.
36. Tu, C.-C., et al., *Surface passivation dependent photoluminescence from silicon quantum dot phosphors.* Opt. Lett., 2012. 37(22): p. 4771-4773.
37. *Print Preview.* Nature, 2012. 487(7405): p. 6-6.
38. Wittbrodt, B.T., et al., *Life-cycle economic analysis of distributed manufacturing with open-source 3-D printers.* Mechatronics, 2013. 23(6): p. 713-726.

39. Falconer, J. *Ultimaker 2 3D Printer Pushes the Limits of Speed and Accuracy*. Gizmag 2013,[cited 2013 November]; Available from: http://www.gizmag.com/ultimaker-2-3d-printer-speed-accuracy/29268/.
40. *World's First 3D Printed Metal Gun Manufactured by Solid Concepts*. Solid Concepts 2013,[cited 2013 November]; Available from: http://www.solidconcepts.com/news-releases/worlds-first-3d-printed-metal-gun-manufactured-solid-concepts/.